

UNIVERSITY OF NOTTINGHAM
SIR PETER MANSFIELD IMAGING CENTRE
SCHOOL OF PHYSICS AND ASTRONOMY

**Developing Techniques for Quantitative Renal Magnetic
Resonance Imaging**

Author:
Alexander James Daniel MSci

Supervisor:
Prof. Susan Francis

15th March, 2021



Thesis submitted to the University of Nottingham for the degree of Doctor of Philosophy

It's very hard to talk quantum using a language originally designed to tell other monkeys where the ripe fruit is.

Terry Pratchett, *Night Watch*

Abstract

Science will happen, but this bit can be read by muggles on ‘tinterweb.

Contents

Abstract	ii
Contents	iii
Acknowledgments	viii
Abbreviations	ix
1 Introduction	1
1.1 Imaging in the Clinic	1
1.2 Clinical Motivation	2
1.3 Thesis Overview	6
1.4 References	8
2 Principles of Nuclear Magnetic Resonance Imaging	11
2.1 Source of the NMR Signal	13
2.1.1 Nuclear Spin	13
2.1.2 Application of an External Magnetic Field	14
2.1.3 Precession	15
2.1.4 Resonance	16
2.2 Relaxation and Contrast Mechanisms	18
2.2.1 Longitudinal Relaxation (T_1)	18
2.2.2 Transverse Relaxation (T_2 and T_2^*)	20
2.2.3 Dipole-Dipole Interactions	25
2.2.4 Diffusion Imaging	27
2.2.5 Optimisation of Tissue Contrast	29

2.3	Forming an Image	31
2.3.1	Signal Localisation	31
2.3.2	Image Acquisition Acceleration	38
2.3.3	Image Acquisition Schemes	40
2.4	Conclusion	46
2.5	References	47
3	Assessment of Renal T_2 Mapping Methods	48
3.1	Introduction	50
3.2	Methods	52
3.2.1	Data Acquisition	52
3.2.2	Post Processing	59
3.2.3	Assessment of Data	60
3.3	Results	66
3.3.1	Fitting Methods	66
3.3.2	Phantom Verification	68
3.3.3	In-Vivo	73
3.4	Discussion	77
3.5	Conclusion	82
3.6	Acknowledgements	82
3.7	References	83
4	Quantitative Methods to Measure Renal Oxygenation	89
4.1	Introduction	91
4.2	Methods	94
4.2.1	Susceptibility-Based Oximetry	94
4.2.2	T_2 Relaxation Under Spin Tagging	96
4.2.3	Inducing Changes in Oxygenation of Blood in the Renal Vein	102
4.3	Results and Discussion	104
4.3.1	Susceptibility-Based Oximetry	104
4.3.2	T_2 Relaxation Under Spin Tagging	106
4.4	Conclusions and Future Work	114

4.5	Acknowledgements	114
4.6	References	115
5	Automated Segmentation of Kidneys using Machine Learning	120
5.1	Introduction	122
5.2	Neural Networks for Image Segmentation	125
5.2.1	Artificial Neural Networks	125
5.2.2	Convolutional Neural Networks	128
5.3	Methods	131
5.3.1	MRI Data Acquisition	131
5.3.2	Manual Segmentation	132
5.3.3	Automated Segmentation Using a CNN Architecture .	132
5.3.4	Statistical Analysis	135
5.4	Results	137
5.4.1	Characteristics of the Training Cohort	137
5.4.2	Reducing Acquisition Time	138
5.4.3	Accuracy of Manual Segmentation	139
5.4.4	Network Testing	142
5.5	Discussion	149
5.5.1	Evaluation of Methodology	150
5.5.2	Future Directions	152
5.6	Conclusions	155
5.7	Acknowledgements	155
5.8	References	156
6	Ex-Vivo Renal MRI	162
6.1	Introduction	164
6.1.1	Validation of Multiparametric MRI via a Nephrectomy Model	164
6.1.2	Assessment of Allograft Viability	167
6.1.3	Ex-Vivo Protocol Aims	169
6.2	MRI Protocol Development	170
6.2.1	Anatomical Scans	172

6.2.2	T_1 Mapping	173
6.2.3	T_2 Mapping	176
6.2.4	T_2^* Mapping	178
6.2.5	Apparent Diffusion Coefficient Mapping	181
6.2.6	Diffusion Tensor Imaging	185
6.3	Depth Based Analysis of Renal Data	194
6.4	Monitoring Changes in MR Parameters Post Fixation	198
6.5	Correlating MRI Measures with Histology in Kidneys of Differing Ages	202
6.6	Conclusion of Future Work	205
6.7	Acknowledgements	207
6.8	References	208
7	Conclusion	217
A	Tractography Pipeline	218

Todo list

■ Make sure these are in the correct order	6
■ Due to stimulate echoes?	57
■ Would a 2D example of applying a Gaussian blur to an image be helpful here too?	63
■ Better word than global for measures of whole body rather than specific organ?	168
Figure: Individual b-values	184
■ stagger slightly so error bars are visible	201

Chapter 6

Ex-Vivo Renal MRI

Abstract

Despite recent developments in quantitative renal Magnetic Resonance Imaging (MRI) the current clinical standard for diagnosis of renal pathologies is limited to biopsy followed by histology, an invasive procedure that is not without risks and highly susceptible to sampling bias. To aid the clinical adoption of renal MRI the interplay between the newly developed MRI protocols and existing histological pipelines must be better understood.

By scanning subjects who are due to undergo a nephrectomy as part of their standard clinical care, the same kidney can be imaged in-vivo using state of the art protocols prior to the operation. Once the kidney has been removed, it can be imaged ex-vivo in exquisite detail to collect the highest quality of MRI data, this can then be correlated to existing histological analysis. These three complimentary streams of data will lead to a better understanding of the MRI parameters and lend confidence to quantitative MRI in the clinic. In future the ex-vivo MRI protocol could also be used to assess the viability of kidney grafts prior to transplant. Here a matched ex-vivo and in-vivo multiparametric renal MRI protocol and advance analysis methods are developed.

This work was presented at the International Society of Magnetic Resonance in Medicine (ISMRM) 27th Annual Meeting, 2019 [1] and United Kingdom Kidney Week (UKKW) 2019 [2]. The bespoke analysis pipelines and software developed here were heavily drawn upon in the development of The United Kingdom Renal Imaging Network (UKRIN) Kidney Analysis Toolbox (UKAT) [3]. This work has also been accepted to be presented at the ISMRM 29th Annual Meeting, 2021, [4].

6.1 Introduction

A recurring theme in renal Magnetic Resonance Imaging (MRI) studies is the limitations imposed by respiratory motion. Sequences must either be optimised and accelerated to fit within a breath-hold, be hugely slowed down through the use of respiratory triggering or accept the motion artefacts that are inevitable during free-breathing acquisition. Additionally the common trade-off in MRI between voxel size, Field Of View (FOV) and acquisition time becomes all the more limiting within the constraints of respirator motion. While these issues are ever-present in day-to-day clinical practice, they also impeded progress, and ultimately, clinical adoption, of techniques in the research phases of their development. Often in research, it is desirable to acquire data of higher quality than would be required in clinical practice. This can be to gain a better understanding of the spacial variance within small structures or acquire best case scenario data with many averages or time points to compare to existing, non-imaging diagnostic techniques.

In this chapter, techniques for ex-vivo renal MRI are developed. These allow research to be conducted without the limitations imposed by respiratory motion and, in future, could be used in the clinic to assess allograft viability prior to transplant.

6.1.1 Validation of Multiparametric MRI via a Nephrectomy Model

Blood and urine tests are commonly used to assess renal health and function however, these are indirect measures and give no indication as to the health of individual kidneys. Consequently, the gold standard in renal diagnostics is a biopsy followed by histological analysis. During a renal biopsy, an area on the patient's back is injected with local anaesthetic then, using ultrasound as a guide, a biopsy needle is inserted into the kidney to remove a

6.1. Introduction

sample of the tissue. Acquiring the biopsy takes approximately half an hour. After the sample is removed the patient is then asked to lie in bed for several hours to minimise the risk of internal bleeding. In approximately 1% of patients, the bleeding caused will require a blood transfusion and approximately 0.5% of patients will require embolisation. While these risks are relatively small, the procedure is still an invasive, destructive and time consuming one for the patient thus making it poorly suited for longitudinal monitoring of renal health. Additionally, this method of biopsy is not viable for some patients such as those with coagulopathy or thrombocytopenia due to the increased risk if a hemorrhage occurs or those that are unable to lie prone such as patients who are intubated for respiratory assistance [5]. While techniques such as the transjugular renal biopsy have been developed (albeit accidentally after taking a wrong turn at the portal vein while trying to acquire a liver biopsy [6]) to serve these patients, this is a more technically complicated procedure. Finally, the samples acquired via biopsy are very small and thus are often not representative of the entirety of the kidney biopsied, let alone both kidneys.

These drawbacks have provided the incentive for the development of multiparametric renal MRI protocols which could prove to be advantageous for both clinicians and patients. A key aspect in the widespread adoption of MRI into renal clinical practice, is a full understanding of the interplay between the current histological pipelines and the newly developed MRI measurements. While it is possible to correlate biopsy results with MRI findings and gain some information as to how different MRI measurements vary with tissue properties, this paradigm still suffers from the small tissue sampling volumes outlined above and the inherent difficulties of in-vivo MRI data acquisition [7]. An alternative paradigm is to scan the kidney in-vivo to collect typical renal MRI data, scan the organ ex-vivo to acquire exquisite MRI data of a far higher quality than would be possible in-vivo, then perform whole organ histology on the tissue. These three streams of complimentary data, all acquired from the same organ, eliminate the large issues with currently implemented paradigms, while still being able to reference the data back to clinically feasible

6.1. Introduction

measures.

One of the first works correlating multiparametric MRI with renal histology was by Inoue *et al*, who found a statistically significant correlation between fibrosis area, as determined from a renal biopsy stained with Masson's trichrome, and Apparent Diffusion Coefficient (ADC) and T_2^* in 37 Chronic Kidney Disease (CKD) patients [8]. This was confirmed by Zhao *et al*, who found a strong correlation between ADC of both the renal cortex and medulla and histopathological fibrosis score on 25 more CKD patients [9]; this study used a more comprehensive histopathology protocol. Feng *et al* also found a correlation between glomerulosclerosis, fibrosis, Fractional Anisotropy (FA) and ADC in CKD subjects [10]. Friedli *et al* found a significant correlation between cortical-medullary differences in T_1 and ADC and fibrosis, this was first found in rats, including histology of whole organs rather than just biopsy samples [11]. The same group then validated this finding in 164 human subjects, correlating with biopsy rather than whole organ [12].

Outside the renal community, work has been done with registered whole-mount histology and both in-vivo and ex-vivo MRI. Jafari *et al* have performed volume matched ex-vivo Quantitative Susceptibility Mapping (QSM) and T_2^* mapping with whole explant histopathology in the liver using the histopathology results to validate predictions of fibrosis using MRI [13]. The University of British Columbia group have carried out extensive work correlating histopathology of whole prostatectomy samples with in-vivo MRI [14, 15]. The same group have also made use of ex-vivo scanning techniques to correlate histopathology with 3T in-vivo data and 7T narrow-bore ex-vivo data [16]. The use of matched histology and MRI data is well established in the neuroimaging field [17] with studies correlating histopathology with diffusion measures [18–21], magnetisation transfer [22, 23], QSM [24, 25] and relaxometry measures [26, 27]. Additionally, post processing packages have been developed to enable accurate registration of whole mount histopathology and MRI data [28, 29].

6.1. Introduction

Thus far, no work has been found comparing whole organ renal histology to in-vivo and ex-vivo MRI measurements. The ideal paradigm for this work is to scan patients who are undergoing a nephrectomy as part of their standard clinical care. Briefly, this method would involve scanning a subject pre-operation to acquire a multi-parametric quantitative MRI dataset. The subject will then have part of their kidney removed, cancerous tissue will be sent for standard lab tests however, non-cancerous tissue will be immersion fixed in formalin. Equivalent scans assessing the same quantitative parameters as were collected in-vivo will be repeated ex-vivo, however these scans will be at a much higher resolution. Finally, the tissue will be sliced for multi-stain histopathology. This pipeline enables the comparison of tried and tested histological staining that clinicians are used to, albeit with larger sample sizes, with in-vivo quantitative MRI data; ex-vivo data acts as an intermediary between histology and in-vivo MRI data.

Given the purpose of this paradigm is to compare pre-existing histological analysis with newly developed, but previously documented renal MRI protocols, the area that will need the most development is the use of ex-vivo MRI to image renal tissue.

6.1.2 Assessment of Allograft Viability

Availability of transplant kidneys is a major limiting factor in the treatment of many patients with end-stage kidney disease. This results in long times on recipient waiting lists incurring additional risks to the patient from the adverse effects of dialysis upon the body and resulting in higher costs to health services.

Despite the shortage of donor kidneys, a significant proportion of those donated are discarded rather than transplanted. This is due to an understandably cautious approach to acceptance of organs from older donors or those with co-morbidities. However these discarded organs will inevitably contain

6.1. Introduction

a range of organ qualities, some of which could have been viable grafts. One method of increasing the number of available organs for transplant is reduce the proportion of discarded kidneys while also avoiding transplanting unviable grafts. To try and assess the viability of marginal organs two methods have been developed using data from the United Kingdom and United States transplant registries. These methods both produce a risk index which is designed to give 1 for a healthy 40 year old donor with an index of less than 1 indicating a lower risk donor and an index higher than 1 indicating a higher risk donor. The United Kingdom Kidney Donor Risk Index (UKKDRI) is given by an empirically derived equation based on the risk factors of donor age, history of hypertension, donor weight, days in hospital and the use of adrenaline [30] while the United States Kidney Donor Risk Index (USKDRI) adds an additional ten risk factor to its model [31]. Receiver Operating Characteristic (ROC) analysis of both methods showed an Area Under Curve (AUC) of 0.62 and 0.63 for UKKDRI and USKDRI respectively, indicating that the models have limited predictive ability. Model accuracy could likely be improved by including measures specific to the kidneys themselves rather than simply demographic and global clinical factors.

Between 2009 and 2013 64.8% of kidney donations came from deceased donors rather than living donors [32]. As these donations are unplanned, there is a significant time period between kidney availability and surgery while a recipient is found, during this time tests could be run on the kidney to assess its viability. One possible modality for such tests is MRI.

By developing a quantitative ex-vivo renal MRI protocol, the health of the kidney to be transplanted could be assessed while a recipient is being found. MRI is ideally suited due to its non-destructive, whole organ coverage, thus avoiding the sampling bias outlined as an issue with biopsy. The results from the MRI exam could be used to improve accuracy of the donor risk index and thus would result in a lower rate of discarded organs and an increase in long term successful grafts.

Better word than global for measures of whole body rather than specific organ?

6.1. Introduction

In addition to scanning the organ ex-vivo, an in-vivo protocol could be used to assess graft function post transplant. By proactively identifying the onset and progression of graft dysfunction, treatment could be modified to extend the life of the transplant.

6.1.3 Ex-Vivo Protocol Aims

To enable research into these topics, a range of ex-vivo acquisition techniques with matched in-vivo counterparts was developed. Keeping the motivations outlined above in mind, the following aims and constraints were imposed on the protocol.

Hardware: Both the in-vivo and ex-vivo protocol should be able to run on readily available hospital hardware. Although some hospitals are linked to the research institutions with access to pre-clinical MRI facilities, this is not the norm. Therefore the protocol should be implemented on human whole body scanners. Additionally, the use of bespoke Radio Frequency (RF) coils should be avoided, while these may deliver superior Signal to Noise Ratio (SNR) they are not readily available.

Acquisition Time: Without the limits on acquisition time imposed scanning subjects, total protocol times can easily become very long. While it is commonplace in pre-clinical settings to scan samples for more than a day, this is not practical on a busy human scanner, especially in a hospital environment. As such, the ex-vivo protocol should be limited to five hours and the in-vivo protocol limited to the standard of one hour.

Time Dependence: Logistics of surgery are complicated with delays and rescheduling of procedures being relatively common occurrences. This combined with the addition of a complicated research protocol has the potential

6.2. MRI Protocol Development

to reduce throughput of samples. To this end, the time dependence of the ex-vivo aspect of the protocol should be minimised so that delays in organ transport or scanner availability do not have a knock on effect on data acquired. In the case of the nephrectomy paradigm, this could be achieved by fixing renal tissue prior to imaging.

6.2 MRI Protocol Development

Imaging was performed on a 3T Philips Ingenia system as 3T scanners are available in most European/North American hospitals however some protocols were also developed for a 7T Philips Achieva system to assess the best case scenario ex-vivo images that could be acquired on human scanners, all in-vivo imaging was performed at 3T. Ex-vivo samples were scanned in 32 channel head coils, Figure 6.1, as these coils allowed for a whole organ to be imaged while also keeping array elements as close to the sample as possible. In-vivo imaging utilised a 16-channel anterior coil array and 16-channel posterior coil array.



Figure 6.1: A sample sat within the 32 channel 3T head coil.

One of the aims of the ex-vivo protocol is to minimise time outside the body as a confounding factor. This enables a greater degree of flexibility with regards to scan times and order of scans within the protocol. Tissue degradation occurs relatively quickly after removal from the body and as such

6.2. MRI Protocol Development

the tissue was fixed to minimise this process. Samples were transported in Phosphate-buffered Saline (PBS) then transferred into ten times the samples volume of 10% Neutral Buffered Formalin (NBF) for twenty four hours. After fixation the samples were washed and rehydrated with PBS and remain in this solution while being scanned to minimise susceptibility artefacts that would be too substantial if the sample were scanned either in air or the NBF. All samples were scanned at room temperature ($\sim 20^{\circ}\text{C}$).

Development work was performed on porcine kidney samples as these are an excellent analogue for human kidneys. Initially, samples were acquired from a local slaughterhouse however these samples were of variable quality. This was largely due to the legislation surrounding animals destined to enter the human food chain. If any part of the animal is to be consumed by humans, the carcase must be thoroughly inspected before any tissue can be released. This causes two problems. As part of the inspection, the kidneys need to be examined, this is done by making an incision in the organ, however the quality of this incision can vary massively with some samples having a neat 20 mm slice cut into them while others are roughly cut in half. The second issue is caused by the variable time between slaughter and the tissue being released after inspection. No preservation techniques, such as storing the kidneys on ice, are employed during the wait for tissue release and as such, the tissue can begin to degrade in this variable and unknown time period.

These issues meant later samples were procured from University of Nottingham Veterinary Science department. The animals slaughtered here are not destined for human consumption and as such the kidneys can be placed into NBF far quicker, additionally the kidneys do not need to be sliced open for inspection. The differing quality of samples acquired from the slaughterhouse and Veterinary Science can clearly be seen in Figure 6.2. The collaboration with Veterinary Science also enables the procurement of a more diverse range of samples such as kidneys from pigs of different ages and therefore different degrees of fibrosis or from animals with induced Acute Kidney Injury (AKI).

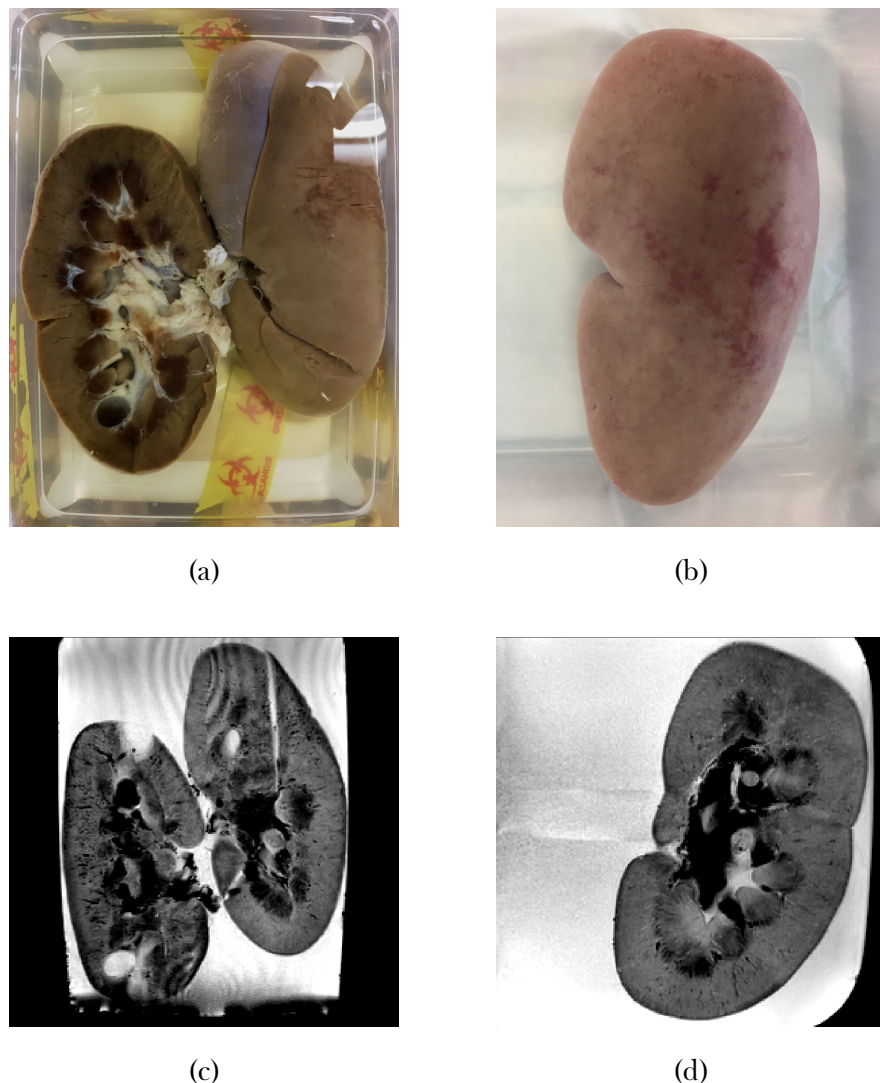


Figure 6.2: (a) A sample procured from the slaughterhouse after it has been fixed. The left hand kidney has been sliced in half; the right hand kidney has the incisions from the meat inspector clearly visible. (b) A sample procured from Veterinary Science post fixation. (c) A T_2 weighted Gradient Echo (GE) acquisition with $TE = 40$ ms of a kidney procured from the slaughterhouse. (d) A T_2 weighted GE acquisition with $TE = 40$ ms of a kidney procured from Veterinary Science.

6.2.1 Anatomical Scans

To make use of the layer based analysis techniques outlined in Section 6.3 and calculate Total Kidney Volume (TKV) a high resolution, whole kidney

6.2. MRI Protocol Development

coverage anatomical scan is required to segment the kidney from surrounding tissue/PBS. In-vivo, the T_2 weighted structural scan from Chapter 5 is used. The ex-vivo protocol is outlined in Table 6.1; this scan was also used to plan subsequent ex-vivo scans.

Parameter	3T Ex-Vivo	3T In-Vivo
Voxel Size	1 x 1 x 1	1.5 x 1.5 x 5
FoV	192 x 192 x 60	350 x 350 x 71
Acquisition Mode	3D	M2D
TE	3.7	60
TR	8.1	1300
Flip Angle	15	90
Bandwidth	191.5	792.3
NSA	1	1
Fold-over Suppression Oversampling	N/A	150
Sense	2 RL, 2AP	2.5
Halfscan	0.625	N/A
Fast Imaging Mode	TFE	TSE
TFE Factor	143	N/A
Shot Interval	4000	N/A
Acquisition Time	53 sec	17 sec (1 x BH)

Table 6.1: Acquisition parameters for anatomical scans.

6.2.2 T_1 Mapping

T_1 mapping protocols were developed for both 3T and 7T systems using an ultrafast gradient echo inversion recovery scheme. The basics of this sequence and T_1 mapping are outlined in Section 2.2.1. An example of the acquisitions at each inversion time is shown in Figure 6.3. The sequence parameters at both 3T and 7T are shown in Table 6.2.

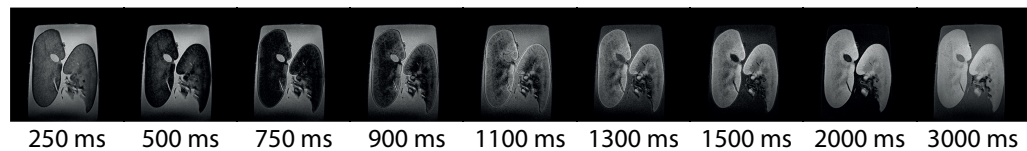


Figure 6.3: Acquisitions at each of the Inversion Time (TI) at 7T.

6.2. MRI Protocol Development

Parameter	3T Ex-Vivo	7T Ex-Vivo	3T In-Vivo
Voxel Size	0.7 x 0.7 x 1.0	0.6 x 0.6 x 0.6	3 x 3 x 5
FoV	160 x 160 x 50	192 x 170 x 24	288 x 288 x 25
Acquisition Mode	3D	3D	MS
TE	5.1		27
TR	11		5000
TI	400, 500, 750, 900, 1100, 1300, 1500, 2000, 2600	250, 500, 750, 900, 1100, 1300, 1500, 2000, 3000	0, 100, 200, 300, 400, 500, 600, 700, 800, 900, 1000, 1100, 1300
Flip Angle	8	8	90
Bandwidth	134.4		39.3
NSA	1	2	1
Fold-over Suppression Oversampling	75	N/A	N/A
Sense	2.5 RL, 1 AP	2 RL, 1.5 AP	2.3
Halfscan	N/A	N/A	0.851
Fast Imaging Mode	TFE	TFE	EPI
TFE Factor	64	240	N/A
Shot Interval	3000	8000	N/A
Acquisition Time	1 hr 20 min 20 sec		1 min 10 sec (Trig)

Table 6.2: T_1 mapping protocols and 3T and 7T.

After a 180° inversion, the signal sampled at each inversion time is proportional to the modulus of the true longitudinal magnetisation, as such, the true dynamic range of the inversion recovery is not sampled. This factor means there is ambiguity as to the polarity of signals near the null point (zero crossing) and can lead to a decreased accuracy when fitting for T_1 as any algorithm is essentially having to fit an extra parameter in the form of the null point.

If the phase of the signal has been saved, the polarity of the magnitude can be corrected using the methods of Szumowski *et al* [33] thus increasing accuracy by increasing dynamic range and removing ambiguity as to the location of the null point for each voxel. Phase data is only accurate if partial Fourier acquisition acceleration techniques (Section 2.3.2), known as halfs-

6.2. MRI Protocol Development

can, are not utilised however, because these acceleration methods result in a decreased SNR they would not be used ex-vivo anyway.

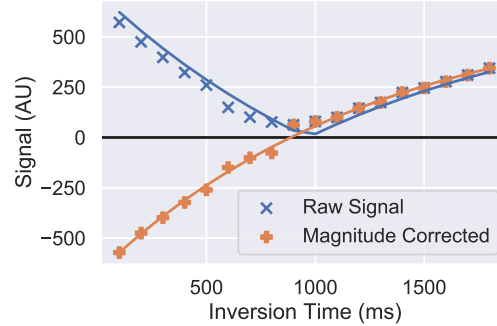


Figure 6.4: The raw signal recorded from a single voxel and the magnitude corrected signal with increased dynamic range.

Once the data has been polarity corrected, a voxel by voxel, least squares trust region reflective method is used to fit the data from each voxel to Equation (6.1) to estimate the T_1 and M_0 of the tissue and an uncertainty in the fit [34].

$$S(TI) = M_0 \left(1 - 2 \cdot e^{-TI/T_1} \right) \quad (6.1)$$

Using these techniques, the T_1 of ex-vivo samples could be calculated at both 3T and 7T, Figure 6.5. For in-vivo acquisitions, halfscan was used and as such magnitude correction could not be employed, thus in-vivo data was fit to the modulus of Equation (6.1).

6.2. MRI Protocol Development

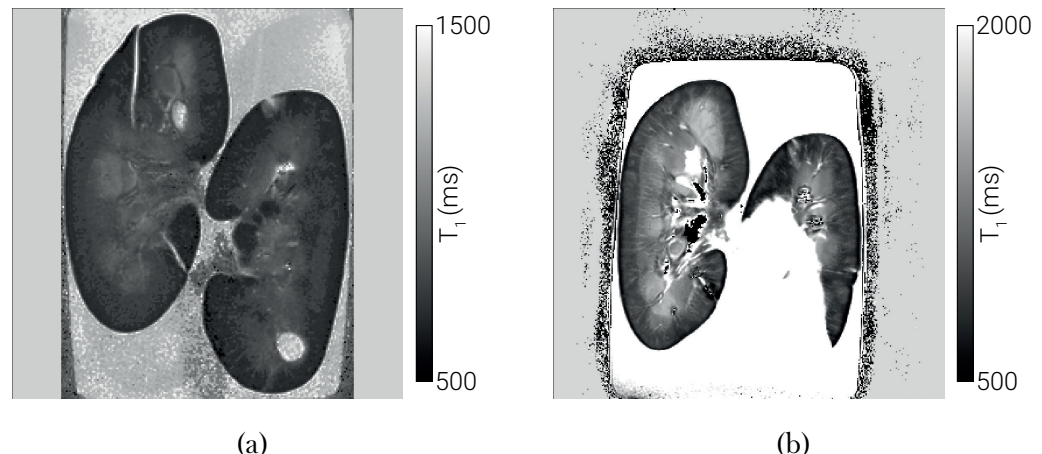


Figure 6.5: Example T_1 maps generated at both 3T (a) and 7T (b).

6.2.3 T_2 Mapping

T_2 mapping makes use of the Gradient Spin Echo (GraSE) sequence developed in Chapter 3. This sequence was only implemented at 3T, an example of the acquisitions at each Echo Time (TE) is shown in Figure 6.6 and the sequence parameters are shown in Table 6.3. The very wide range of TE sampled ex-vivo will enable future multi-exponential analysis of the data allowing for a more accurate quantification of the long T_2 components of the tissue [14, 35].

6.2. MRI Protocol Development

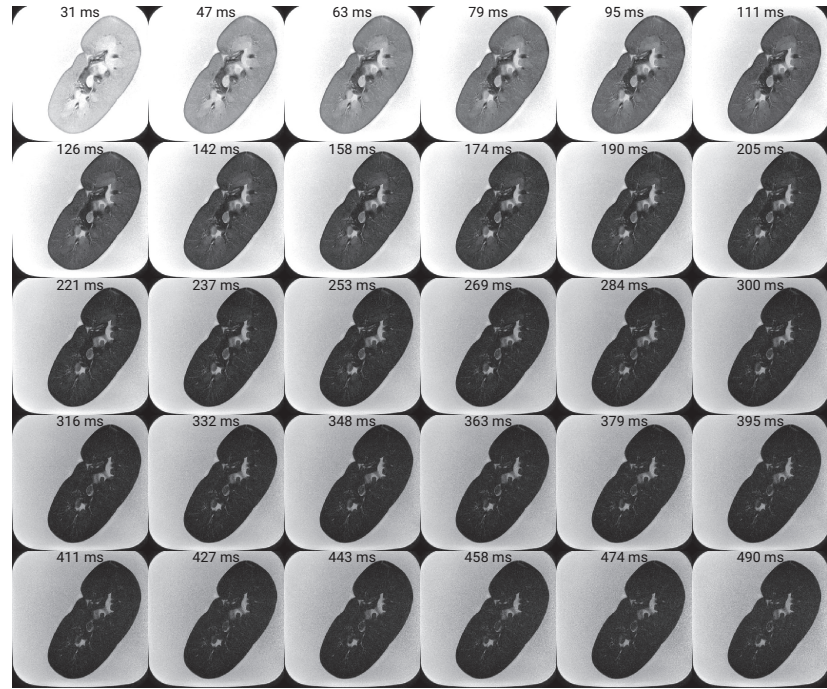


Figure 6.6: Acquisitions of an ex-vivo sample at each of the TE.

Parameter	3T Ex-Vivo	3T In-Vivo
Voxel Size	0.7 x 0.7 x 1.0	3 x 3 x 5
FoV	160 x 160 x 20	288 x 288 x 25
Acquisition Mode	MS	MS
TE	31:15.8:489.9	11:5.6:179
TR	3000	3000
Flip Angle	90	90
Bandwidth	118.9	427.9
NSA	2	1
Fold-over Suppression Oversampling	75	66
Sense	2.55	2.55
Halfscan	N/A	N/A
Fast Imaging Mode	GraSE	GraSE
TFE Factor	30	30
EPI Factor	3	3
Startup Echoes	1	1
Acquisition Time	30 min 30 sec	3 min 9 sec (Trig)

Table 6.3: T_2 mapping sequence parameters.

T_2 maps are generated on a voxel by voxel basis using a least squares trust region reflective method to fit the data to Equation (6.2) and thus estimate T_2

6.2. MRI Protocol Development

and M_0 .

$$S(TE) = M_0 \cdot e^{-TE/T_2} \quad (6.2)$$

As outlined in Section 3.3.1 multiple methods of estimating T_2 were compared with the basic two parameter fit delivering the most desirable results. Using this pipeline, T_2 maps could be generated, an example of which is shown in Figure 6.7. While partial voluming has been minimised by keeping voxel sizes small, the use of multi-exponential fitting models should be explored in future. This would allow the long T_2 components of the signal, such as the signal from PBS to be modelled separately to the renal tissue, thus increasing accuracy.

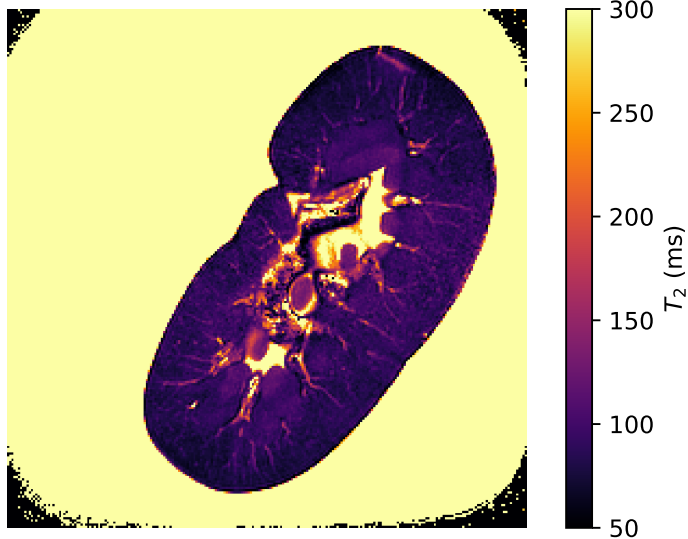


Figure 6.7: An example ex-vivo T_2 map acquired using the scheme above. This sample had been formalin fixed and stored in PBS for multiple months, hence the lack of contrast between cortical and medullary tissue.

6.2.4 T_2^* Mapping

T_2^* acquisition is performed using a simple multi-slice gradient echo sequence as outlined in Section 2.2.2 and was developed at both 3T and 7T. The acquisition parameters are shown in Table 6.4. In addition to the magnitude data saved for T_2^* mapping, the phase data is also saved to allow a QSM

6.2. MRI Protocol Development

pipeline to be developed in future.

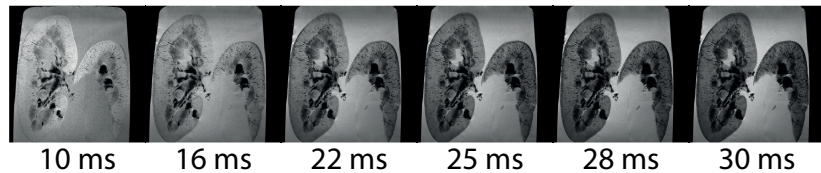


Figure 6.8: Acquisitions at each of the TE at 7T.

Parameter	3T Ex-Vivo	7T Ex-Vivo	3T In-Vivo
Voxel Size	0.7 x 0.7 x 1.0	0.5 x 0.5 x 1	1.5 x 1.5 x 5
FoV	160 x 160 x 25	145 x 145 x 10	288 x 288 x 25
Acquisition Mode	MS	MS	MS
TE	15:5:50	10, 13, 16, 19, 22, 25, 28, 30	5:3:38
TR	697		79
Flip Angle	38	38	25
Bandwidth	35 - 56		1328.6
NSA	1	3	1
Fold-over Suppression Oversampling	75	N/A	144
Sense	2	2	2
Halfscan	N/A	N/A	N/A
Fast Imaging Mode	None	None	None
Acquisition Time	46 min 25 sec		47 sec (3 x BH)

Table 6.4: Acquisition parameters for T_2^* mapping sequences at 3T and 7T.

Estimation of T_2^* can be performed via two different methods, fitting to a two parameter exponential (Equation (6.3)) or performing a weighted linear fit to the natural logarithm of the signal. The latter of these methods is far less computationally intensive and as such, runs much quicker.

$$S(TE) = M_0 \cdot e^{-TE/T_2^*} \quad (6.3)$$

The acquisition parameters of the 3T ex-vivo protocol were simulated to

6.2. MRI Protocol Development

compare the two fitting methods using Monte Carlo techniques. The linear fit produces a slightly greater Coefficient of Variation (CoV) than the exponential fit at lower T_2^* , Figure 6.9a. Additionally, the relative error, defined by Equation (6.4), has a greater magnitude below 20 ms when fitting with the linear fit than the exponential fit, Figure 6.9b. The T_2^* we expect from the kidneys at 3T is greater than 20 ms so in the interests of computational efficiency, the linear fitting method was used.

$$\text{Relative Error} = \frac{t_2^* \text{ fit} - t_2^* \text{ simulated}}{t_2^* \text{ simulated}} \quad (6.4)$$

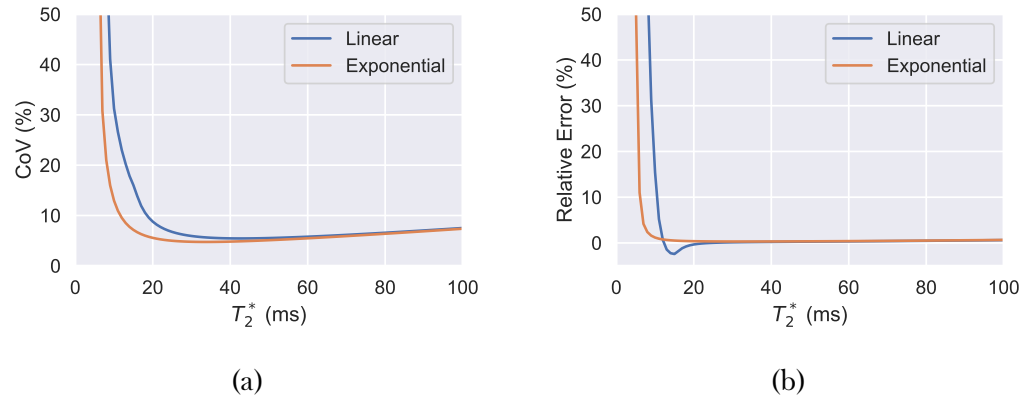


Figure 6.9: Simulations to ascertain the accuracy of each T_2^* fitting algorithm over a range of T_2^* .

Using the acquisition and post processing steps above, T_2^* maps can be generated, examples of which are shown in Figure 6.10.

6.2. MRI Protocol Development

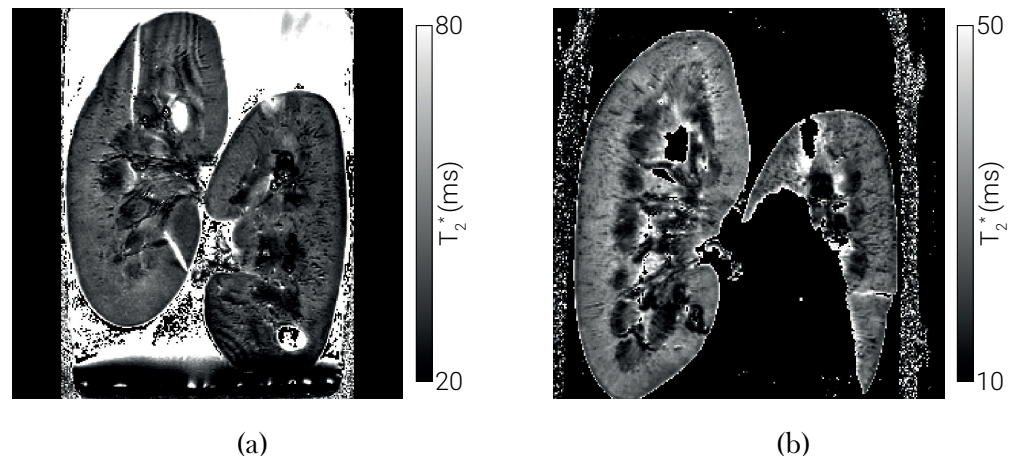


Figure 6.10: An example T_2^* map acquired at 3T (a) and 7T (b) fit using the weighted fit to the natural logarithm of the signal.

6.2.5 Apparent Diffusion Coefficient Mapping

The underlying principles of diffusion imaging are outlined in Section 2.2.4, here Diffusion Weighted Imaging (DWI) is performed using a single shot Spin Echo (SE)-Echo Planar Imaging (EPI) sequence over a range of b-values applied in three orthogonal directions. By acquiring diffusion gradients in three different directions and calculating the mean, the effects of diffusion anisotropy can be minimised. The sequence was developed for 3T systems, sequence parameters are summarised in Table 6.5.

6.2. MRI Protocol Development

Parameter	3T Ex-Vivo	3T In-Vivo
Voxel Size	1.5 x 1.5 x 1.5	1.5 x 1.5 x 5
FoV	160 x 160 x 51	288 x 288 x 25
Acquisition Mode	MS	MS
TE	72	71
TR	1800	1800
b-values	0, 5, 15, 30, 45, 60, 75, 90, 105, 120, 135, 150, 175, 200, 300, 400, 500, 600	0, 5, 15, 30, 45, 60, 75, 90, 105, 120, 135, 150, 175, 200, 300, 400, 500, 600
Flip Angle	90	90
Bandwidth	13.2	13.7
NSA	1	1
Fold-over Suppression Oversampling	75	N/A
Sense	2.3	2.3
Halfscan	0.676	0.676
Fast Imaging Mode	EPI	EPI
EPI Factor	91	83
Phase Encode Direction	L then R	L then R
Acquisition Time	9 min 44 sec	2 min 42 sec (Trig)

Table 6.5: ADC mapping acquisition parameters.

The diffusion sensitising block of the pulse sequence is time consuming and as such necessitates the use of fast image techniques, EPI is the simplest to implement however is not without drawbacks. It suffers from geometric distortions, particularly in the phase encode direction, due to inhomogeneities in the B_0 field cause by susceptibility differences. These geometric distortions can be problematic for this paradigm as the ability to correlate, on a voxel by voxel basis, parameters acquired with different sequences is at the core of multiparametric MRI. Geometric distortions make this impossible. The susceptibility of PBS and renal tissue is similar however there is a very large difference between the PBS and surrounding air and as such, distortions can be problematic.

As the distortions are predominantly in the phase encode direction, by inverting the direction of the phase encode blips, the direction of the distortion can be reversed, Figure 6.11a. By acquiring images with both phase encode

6.2. MRI Protocol Development

directions the underlying field map can be estimated and used to undistort the data [36]. This process can be carried out using fMRIB Software Library (FSL) “topup” however, as this tool was designed for work in the brain, a custom configuration to perform more iterations of the field estimation algorithm with a greater degree of regularisation is required.

Although in some cases it is possible to acquire only the b0 image in both phase encode directions, calculate the displacement field, then apply this field to other b-values, it was decided that the $\sqrt{2}$ SNR increase of acquiring two volumes and averaging them is beneficial. Additionally if, in the case of in-vivo data, there are issues with motion in the b0 volumes, then another diffusion weighting can be used to estimate the displacement, thus adding inherent redundancy to the pipeline.

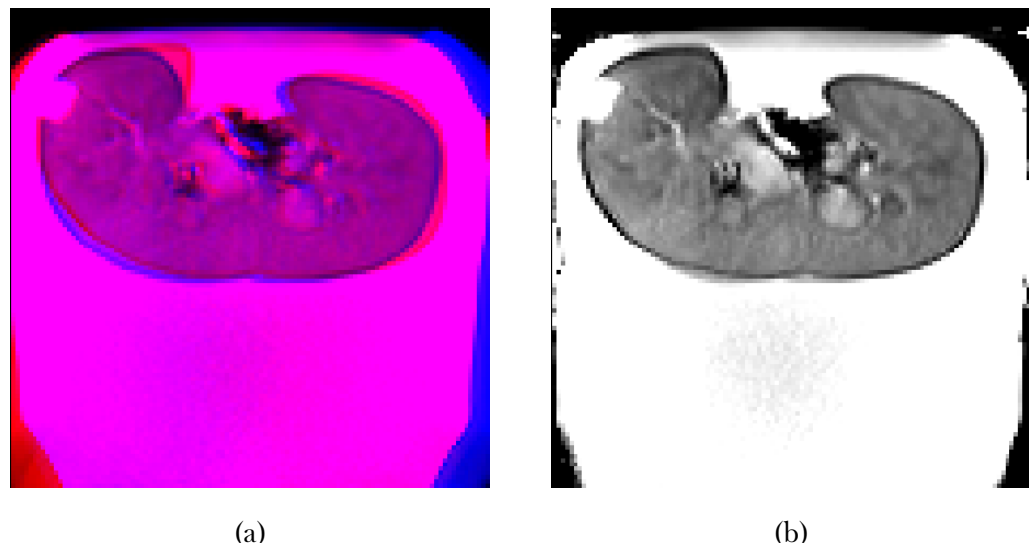


Figure 6.11: (a) b0 images collected with opposing phase encode directions overlay in red and blue. (b) A composite image with EPI distortions corrected using topup.

6.2. MRI Protocol Development

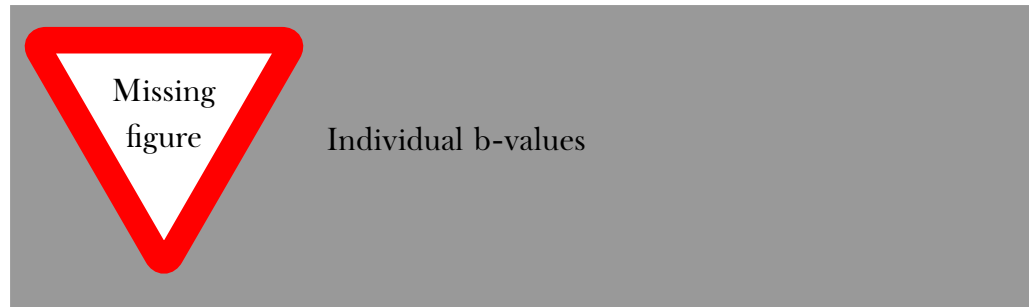


Figure 6.12: Distortion corrected images at each b-value.

The average of the three directions at each b-value and phase encode direction is calculated. EPI distortion correction is performed on both ex-vivo and in-vivo data using topup to enable accurate voxel by voxel comparison of ADC to other quantitative parameters. The natural logarithm of the distortion corrected signal from each voxel over each b-value is taken and a linear least squares fit performed. This enables a quick estimation of ADC and an uncertainty in the fit.

Using these techniques, the ADC of both in-vivo and ex-vivo renal tissue can be calculated, Figure 6.13, with no geometric distortions. Although not implemented here, the large number of low b-values sampled should make estimations of more advance diffusion parameters possible such as fitting the data to an Intravoxel Incoherent Motion (IVIM) model [37].

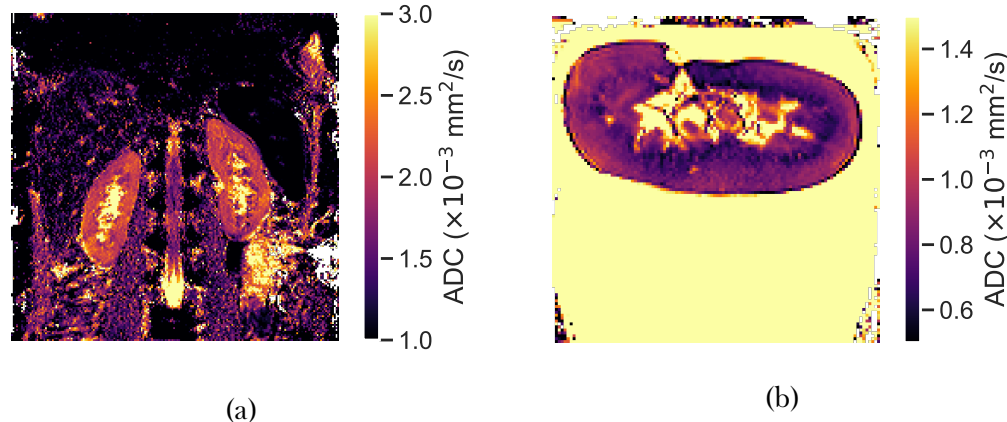


Figure 6.13: ADC maps acquired of both an in-vivo subject (a) and ex-vivo sample (b).

6.2.6 Diffusion Tensor Imaging

ADC maps provide an understanding as to how readily molecules can diffuse through a tissue, however they do not provide any information as to what directions the molecules are travelling, to measure this, Diffusion Tensor Imaging (DTI) is used. The renal group at Sir Peter Mansfield Imaging Centre (SPMIC) had no existing high resolution in-vivo (or ex-vivo) DTI protocol, as such this was specifically developed for this paradigm.

The acquisition scheme used is very similar to that in Section 6.2.5, a single shot SE-EPI scheme with monopolar diffusion gradients. The difference lies in the fact that, rather than acquiring a large range of b-values over three different directions, only a b0 and one other b-value are acquired over a minimum of six directions although in practice, many more. This is known as a single shell DTI scheme. As the diffusivity in, for example, the positive x direction is the same as the negative x direction most DTI schemes acquire a hemisphere of directions, however, to apply additional image deformation correction techniques outlined below, diffusion vectors were acquired over a full sphere, Figure 6.14.

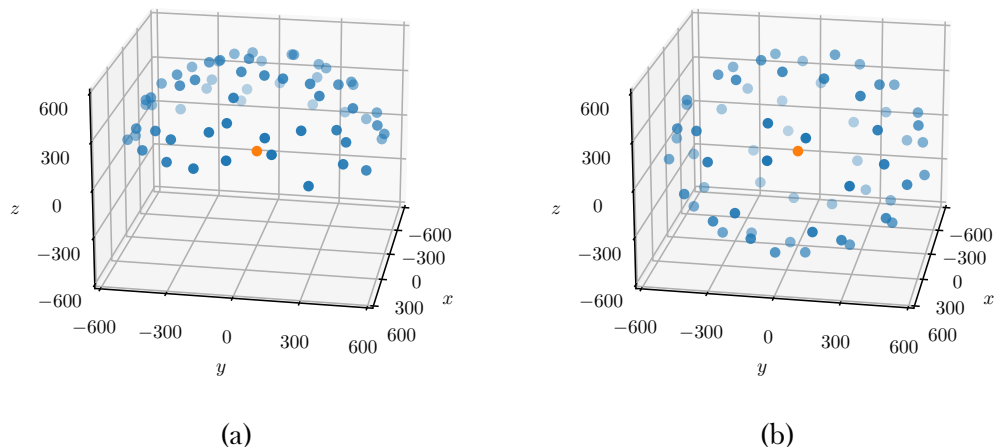


Figure 6.14: (a) 64 diffusion directions acquired over a hemisphere (b) 64 diffusion directions acquired over a full sphere as used in this chapter. b0 is shown in orange with subsequent b-values shown in blue.

6.2. MRI Protocol Development

Mathematically, DTI is estimating the tensor, \mathcal{D} in equation (6.5) where D_{xx} , D_{yy} and D_{zz} represent diffusivity along the x , y and z directions in the lab frame and are equivalent to the three directions sampled in Section 6.2.5. D_{yx} , D_{zx} and D_{zy} represent diffusivity between the principle axis of the lab frame, as \mathcal{D} is symmetric, $D_{yx} \equiv D_{xy}$, $D_{zx} \equiv D_{xz}$ etc, hence DTI can be performed by only sampling a hemisphere of diffusion vectors.

$$\mathcal{D} = \begin{bmatrix} D_{xx} & D_{xy} & D_{xz} \\ D_{yx} & D_{yy} & D_{yz} \\ D_{zx} & D_{zy} & D_{zz} \end{bmatrix} \quad (6.5)$$

Like the ADC sequence, a full dataset is acquired with both opposing phase encode directions to assist with geometric distortion correction. A summary of the sequence parameters is shown in Table 6.6.

Parameter	3T Ex-Vivo	3T In-Vivo
Voxel Size	2.3 x 2.3 x 2.3	3 x 3 x 3
FoV	160 x 160 x 51	288 x 288 x 60
Acquisition Mode	MS	MS
TE	85	82
TR	5100	5100
b-values	0, 600	0, 600
Directions	128	64
Flip Angle	90	90
Bandwidth	17.1	30.5
NSA	2	1
Fold-over Suppression Oversampling	100	N/A
Sense	2	2
Halfscan	0.609	0.609
Fast Imaging Mode	EPI	EPI
EPI Factor	79	47
Phase Encode Direction	L then R	L then R
Acquisition Time	52 min 42 sec	8 min 10 sec (Trig)

Table 6.6: DTI acquisition parameters.

The large number of diffusion directions sampled makes additional geo-

6.2. MRI Protocol Development

metric distortion correction possible. The rapidly switching fields of the diffusion sequence induce eddy currents in the sample, which in turn induce an opposing magnetic field. This leads to off-resonance distortions in the image which are different for each b-vector. To combat this FSLs “eddy” can be used [38]. This tool was developed with the brain data from the Human Connectome Project in mind however [39], here it is successfully used to reduce geometric distortions in ex-vivo and in-vivo DTI data and subject motion in the in-vivo data. The tools performance is optimal when b-vectors are distributed over a full sphere as this results in approximately opposing eddy current distortions and as such, makes estimation of the deformation more accurate.

Once the raw data has been processed with topup and eddy, quantitative maps can be generated. Eigenvalues ($\lambda_1, \lambda_2, \lambda_3$) and eigenvectors ($\epsilon_1, \epsilon_2, \epsilon_3$) are calculated for each diffusion tensor, \mathcal{D} . FA maps can be calculated from equation (6.6). Here it can be seen that if $\lambda_1 = \lambda_2 = \lambda_3$, as is the case for isotropic diffusion, FA tends to 0. An example renal FA map is shown in Figure 6.15a where bright voxels represent areas of higher FA and therefore more anisotropic diffusion.

$$FA = \sqrt{\frac{(\lambda_1 - \lambda_2)^2 + (\lambda_2 - \lambda_3)^2 + (\lambda_1 - \lambda_3)^2}{2(\lambda_1^2 + \lambda_2^2 + \lambda_3^2)}} \quad (6.6)$$

FA can also be used to create fibre direction maps as shown in Figure 6.15b. Here the colour is determined by the direction of the principal eigenvector, ϵ_1 , the primary direction of diffusion, and the brightness is modulated by FA. As the name suggests, these maps provide a visual indication as to the direction diffusion is occurring in a tissue and how strongly it is constrained to that single direction.

The final voxel based map produced using the DTI data is an ADC map, often called Mean Diffusivity (MD) in DTI literature. This is calculated using equation (6.7) and an example is shown in Figure 6.15c. All three of these voxel based maps are generated using FSL.

$$MD = \frac{(\lambda_1 + \lambda_2 + \lambda_3)}{3} \quad (6.7)$$

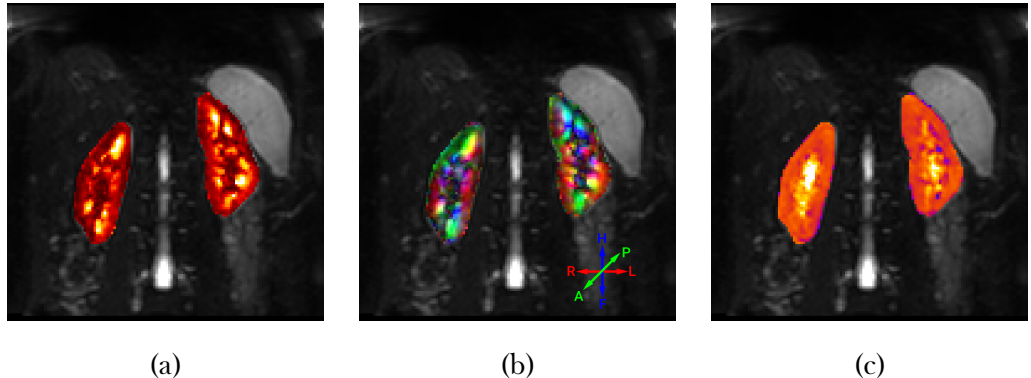


Figure 6.15: FA (a), fibre direction (b) and MD (c) maps generated from the same in-vivo DTI data.

An extension of the fibre direction map is tractography, a technique that can remove the simplification that a voxel has a single direction of diffusion. Even at the highest resolutions achievable with MRI, the biological structures dictating diffusion are orders of magnitude smaller than the resolving power of MRI and as such multiple mechanisms can occur in a single voxel e.g. crossing of neurons or microvascular. In the brain this technique is used to visualise nerve tracts and connectivity within the brain; in the kidneys it can be used to visualise the coherent motion of renal processes. Tractography calculations are performed using the open-source python package Dipy [40] and the resulting tracts are visualised using TrackVis [41].

To model multiple fibres entering and exiting a voxel, a more sophisticated model than simply looking at the principle eigenvector is required. This takes the form of an Orientation Distribution Function (ODF) which can be thought of as the probability a fibre will enter or exit a voxel through a specific solid angle. ODFs can be visualised as isosurfaces where the surface represent all points of equal probability, example ODFs are shown in Figure 6.16. Techniques such as Q-ball imaging [42, 43] and diffusion spectrum imaging [42] can be used to estimate the ODF however these methods tend to require high

6.2. MRI Protocol Development

b-values and as such a lower SNR acquisition making them less suitable to abdominal imaging. Instead a constrained spherical deconvolution method is used [44–46].

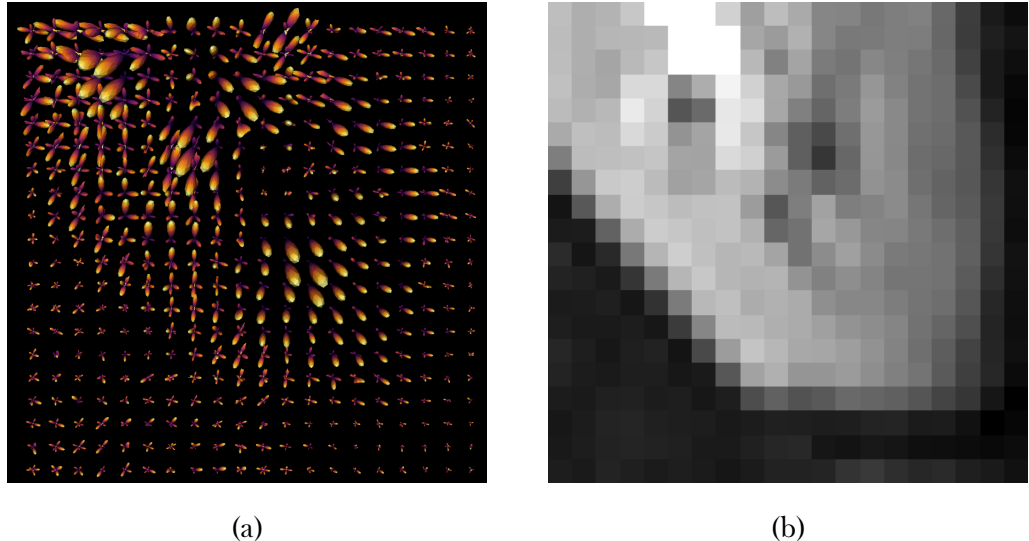


Figure 6.16: The ODFs for a small number of voxels of renal tissue (a) and the corresponding b0 image to help visualise the part of the kidney the data is coming from (b).

The peak values of ODFs are calculated and used to generate streamlines which represent the tracts of coherent diffusion. The calculation of streamline paths is performed using the Euler Delta Crossings (EuDX) method [47]. This tractography pipeline and its many hyper-parameters are best summarised in code form and as such are included in Appendix A. The results of this processing pipeline are tractograms as shown in Figure 6.17.

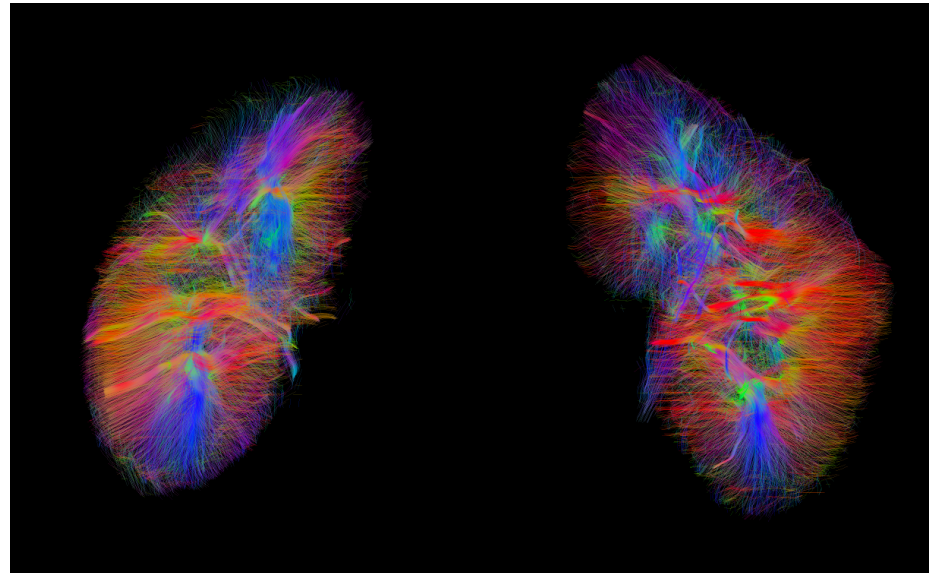


Figure 6.17: Example tractography generated using the above protocol.

As this tractography protocol was developed from scratch, both acquisition and the post processing pipeline were verified in the brain. Tractography is a far more mature technique in neuroimaging and as such, verification that the pipeline produces reasonable results on a more familiar anatomy lends confidence to the tractograms produced of the kidneys. The FOV of the acquisition was adjusted to cover the whole brain but all other parameters were kept constant. The resulting maps and tractogram were all as expected, an example tractogram of the brain produced using this pipeline is shown in Figure 6.18.



Figure 6.18: A tractogram of the brain produced to verify the DTI acquisition and post-processing scheme developed for the kidneys produces expected results within a structure more commonly the subject of tractography.

Renal in-vivo results were compared to those in literature and found to be in agreement [48–50]. Additionally, renal features with a known structure can be observed in the tractograms such as the radial structure of the medullary pyramids, Figure 6.19.

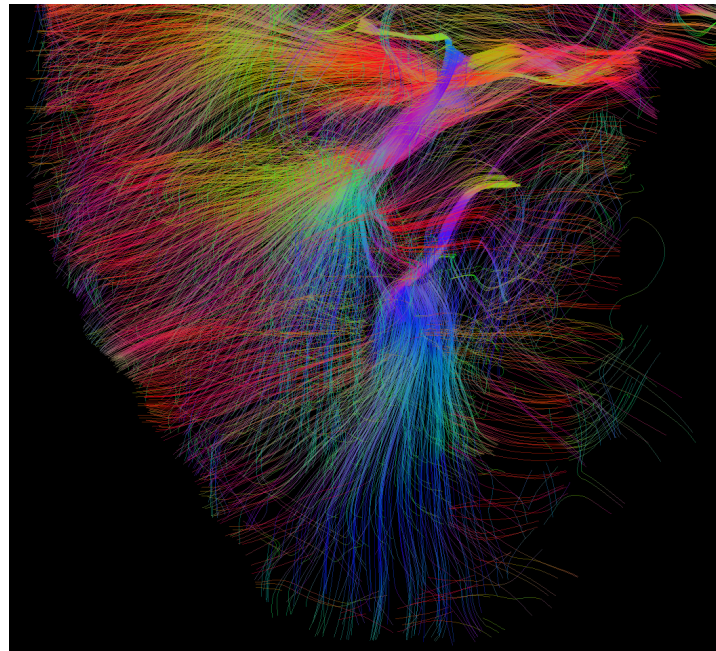


Figure 6.19: The medullary pyramids observed in tractography.

6.2. MRI Protocol Development

An area that still needs further development is the ex-vivo DTI protocol. There are promising early results however ex-vivo diffusion imaging poses additional difficulties. During the fixation process, methyl bridges cross link with proteins within the tissue stiffening it and causing a small amount of shrinkage [51]. This combined with the lower temperatures of ex-vivo samples ($\sim 20^{\circ}\text{C}$ room temperature rather than $\sim 37^{\circ}\text{C}$ body temperature) leads to a reduced degree of diffusion, seen in Figure 6.13. While this results in a higher SNR of diffusion sensitised volumes for a given b-value, the underlying diffusion signal being measured is much smaller i.e. there is less of a difference between b_0 and $b-600 \text{ sec/mm}^2$ and thus the accuracy of the quantitative maps, Figure 6.20, and tractography, Figure 6.21, is reduced.

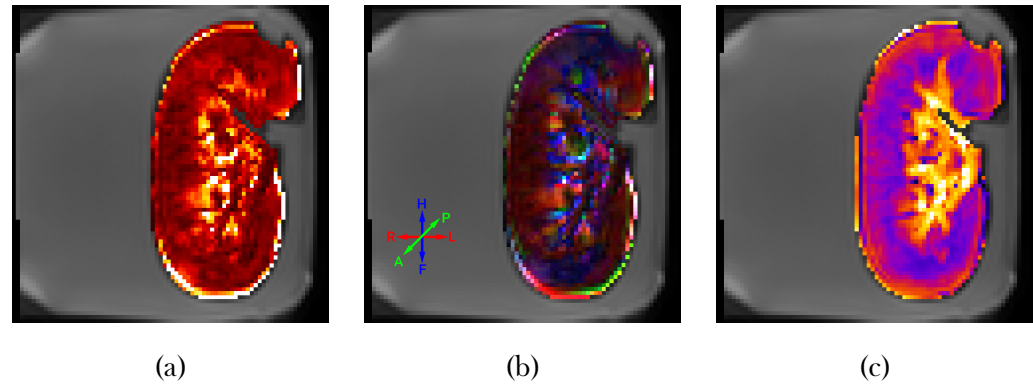


Figure 6.20: FA (a), fibre direction (b) and MD (c) maps of an ex-vivo sample.

6.2. MRI Protocol Development

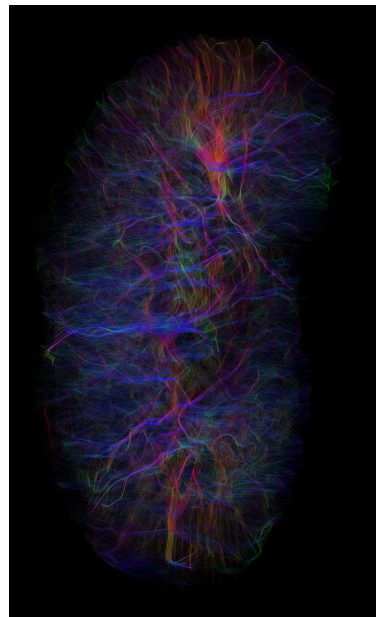


Figure 6.21: Tractography of an ex-vivo kidney sample.

6.3 Depth Based Analysis of Renal Data

The vast majority of analysis of quantitative renal MRI data is based around defining Region Of Interest (ROI) within the kidneys to segment the renal cortex from the medulla and calculate the average of quantitative parameters within these ROI. While this method has provided excellent results, it is by no means perfect. The most common method to define these ROI is manually drawing voxels that represent each tissue type, this can lead to human bias, even if an anatomical scan is used for the segmentation rather than the quantitative map. Automated methods have been proposed, however, as outlined in Chapter 5, these be difficult to generalise.

There is a desire for a more objective and quantitative analysis methodology to complement the quantitative nature of the MRI data acquired. To this end, inspiration has been taken from the analysis pipelines used by neuroimagers who can stratify tissue by layers [52–55]. Although in neuroimaging the layers are designed to mimic the underlying layer based architecture of neuroanatomy, the process of defining equidistant layers from a cortical surface can be applied to the kidneys where renal cortex is found at the surface of the kidney and medulla towards the centre.

The concept of applying layer based analysis to quantitative renal MRI was pioneered by Pruijm and Milani [56–59] in the context of analysis of Blood Oxygen Level Dependent (BOLD) R_2^* mapping, where $R_2^* = 1/T_2^*$. Their method, known as Twelve Layer Concentric Objects (TLCO), uses two user delaminated boundaries, Figure 6.22a, to calculate twelve equidistant layers between the renal pelvis and cortex, Figure 6.22b. These layers can then be applied to an R_2^* map with the average of each layer calculated. The measurements of R_2^* in each layer can be used to estimate $R_{2\text{ outer}}^*$, analogous to cortical R_2^* ; $R_{2\text{ inner}}^*$, corresponding to medullary R_2^* and “slope”, comparable to cortico-medullary difference, Figure 6.22c. This technique is applied to a single, coronal oblique, slice.

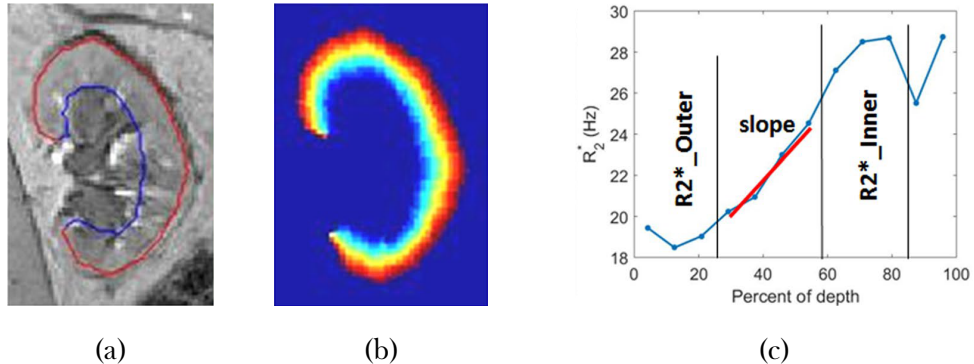


Figure 6.22: Manually defined paths of the inside (blue) and outside (red) of the kidney, (a), are used to generate layers using the TLCO technique (b). Average R_2^* is calculated within each layer and a gradient between outer and inner layers computed (c). Example images are from Li *et al.*, 2019 [59].

As part of a consensus survey, the question “The TLCO or onion peel is a preferred analysis method [for renal BOLD MRI]?” was recently put to an international panel of 24 leading experts in the field of renal BOLD MRI [60]. Only 53% of respondents agreed with the question. The example reason for disagreeing was a preference for true coronal acquisition rather than coronal oblique. This combined with the limitations of a single slice acquisition have lead to the development of the 3D depth based method presented here.

For this analysis method to be applied to quantitative data, a full kidney coverage scan must be acquired, Figure 6.23a, this scan can be of any sequence as long as there is sufficient contrast between the kidneys and surrounding tissue, for example in-vivo the the T_2 weighted Half-Fourier Single-shot Turbo spin Echo (HASTE) scan from Chapter 5 is ideal. The kidneys are then segmented using this scan to generate a binary mask, Figure 6.23b.

Using a bespoke FreeSurfer [61] pipeline, this mask can be converted from the binary voxel based representation into a smooth surface, Figures 6.23c and 6.23d. This surface is made of a very high resolution triangular mesh, Figure 6.23e, and as such allows layers to be calculated at a higher resolution than the original scan. The distance from the centre of each voxel to

6.3. Depth Based Analysis of Renal Data

the closest point on the mesh is then calculated. The sign of this distance i.e. if the point is inside or outside the tissue, is calculated by taking the dot product of the vector from the voxel to the surface and the vector normal to the surface. If the magnitude of the dot product is positive the voxel is outside the surface, if it is negative, it is inside the surface. This results in a quantitative map of the depth of every voxel in the tissue, Figure 6.23f.

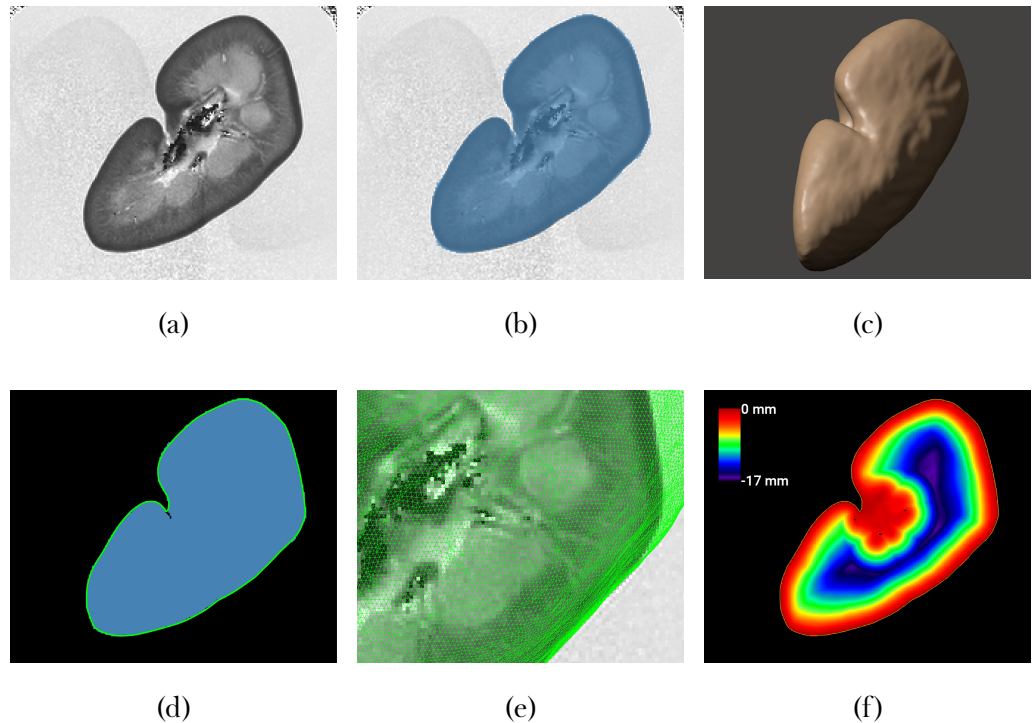


Figure 6.23: (a) The original MRI data with clear contrast between the kidney and surrounding tissue/PBS. (b) A binary mask generated from the image data. (c) The surface representation of the binary mask, note this does not appear blocky as it would if it were simply filled voxels. (d) The green line is the edge of the surface, the blue area is the binary mask, the surface edge is not limited to the voxel grid. (e) The mesh representation of the surface, coordinates of the vertexes of these polygons are used to calculate the distance from each voxel to the surface. (f) A depth map showing how far each voxel is from the surface of the kidney.

The depth map can be quantised to any desired precision e.g. the nearest 1 mm, resulting in layers of voxels equidistant from the surface of the kidney.

6.3. Depth Based Analysis of Renal Data

Using the embedded affine transform of the quantised depth map, these layers can be transformed into the space of any other scan in the same session. This negates the need for quantitative scans to be modified either in FOV to acquire the full kidney, or geometry i.e. the respondents from the survey who don't like acquiring coronal oblique data don't need to. Once the quantised depth map is in the same space as a quantitative map, the average of all voxels in each layer can be calculated.

The 3D nature of this methodology is a major advantage in quantitative renal MRI where it is common to acquire multiple slices of data; using this method all voxels in the kidney can be included in calculations rather than just those of the central slice. By decoupling layer definition from quantitative map acquisition, a greater degree of robustness and flexibility is afforded. With TLCO a not-quite-coronal oblique R_2^* map will produce differing results to a coronal oblique acquisition whereas our method will apply the same layers to the map regardless of acquisition, thus increasing repeatability. This method was applied to analyse samples in Section 6.5.

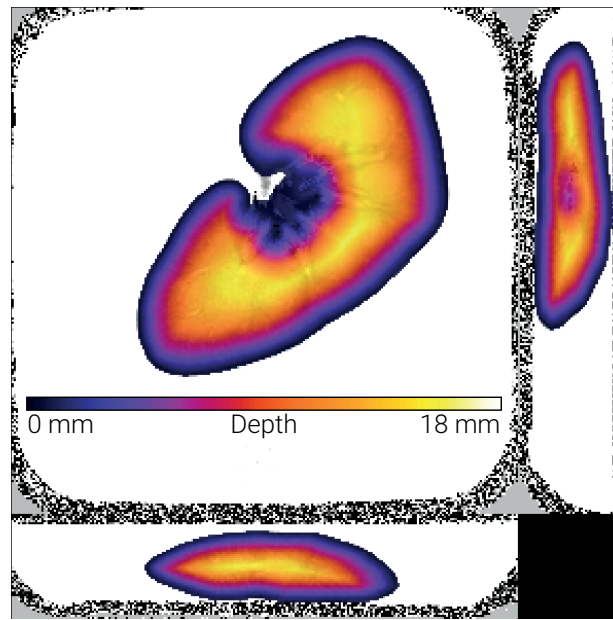


Figure 6.24: An example depth map showing the 3D nature of the layers produced using this technique.

Limitations of this method are the fact it can only be applied to whole

kidneys, in the case of scanning biopsy samples or the kidneys in Section 6.4, this pipeline would lead to highly inaccurate results. It relies on the surface of the sample also being the surface of the kidney; if this assumption does not hold then voxels that are at the surface of the sample will be incorrectly categorised as superficial renal tissue (generally cortex). The computational resources required to run the pipeline are not insignificant, both FreeSurfer and MATLAB are dependencies thus limiting the operating systems the pipeline can be run on and making setup more complicated. Additionally processing times are tens of minutes rather than seconds as is the case for TLCO.

In future a direct comparison of the depth based method outlined above and TLCO should be performed. While the methods are trying to achieve slightly different goals in their definition of layers, a comparison of which produces the most biologically relevant layers could be conducted. The depth based method is a equidistant layering technique, neuroimaging also makes use of equivolume layers [54]. These could also be relevant to renal imaging and should be explored in future.

6.4 Monitoring Changes in MR Parameters Post Fixation

As outlined already, fixation is a necessity step to ensure a consistent protocol and minimise logistical hurdles in having scanners available at specific times when, by the nature of ex-vivo samples, the acquisition process can be somewhat flexible in timings. The effects of fixation on brain tissue have already been reported [62–64] however no literature on the effects of fixation of renal tissue is available. Here we characterise the stability of T_1 and T_2^* in renal tissue post fixation to ascertain how precise the timings of the ex-vivo protocol need to be.

The initial investigation assessed the long term stability of the kidneys by

6.4. Monitoring Changes in MR Parameters Post Fixation

collecting T_1 and T_2^* maps at both 3T and 7T over a ten week period post fixation, the kidneys were stored in PBS for the duration of the experiment. An unfixed kidney was also scanned at 3T. Analysis was performed on the resulting maps by defining a ROI for the cortex and medulla then calculating the mean and standard deviation of the voxels within each ROI. The variation in T_1 and T_2^* can be seen in Figure 6.25. Unfortunately due to technical scanner issues, it was not possible to scan the sample at 7T ten weeks post fixation and the quality of the 3T T_1 acquisition two weeks post fixation was significantly inferior; as such these data points have been omitted from Figure 6.25.

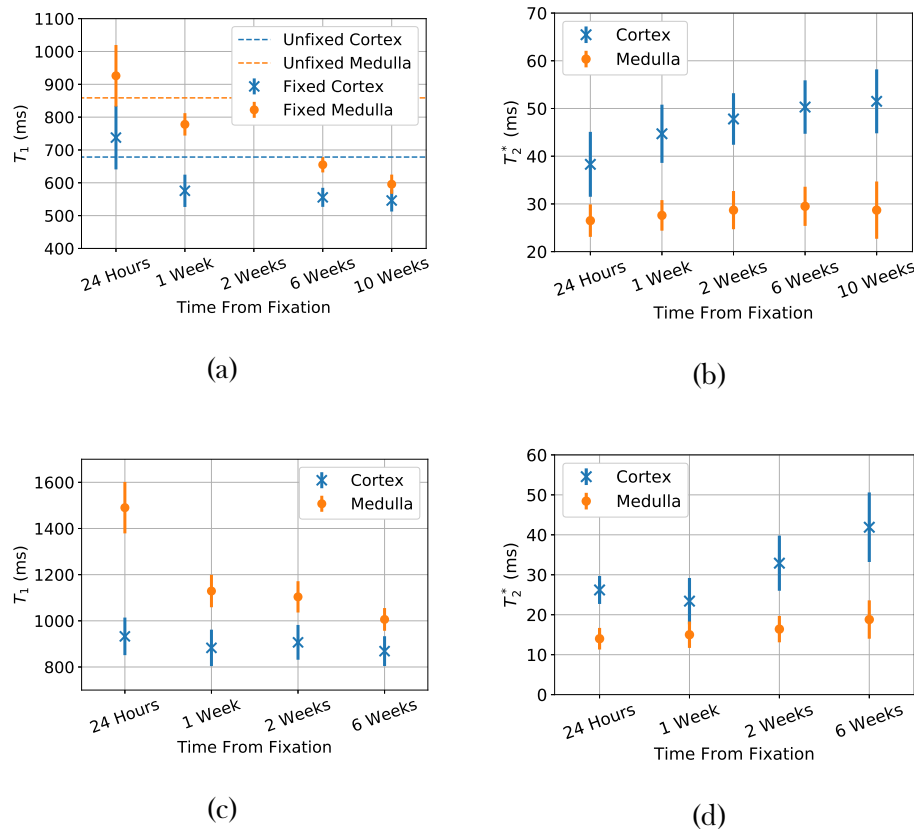


Figure 6.25: Variation in T_1 (a & c) and T_2^* (b & d) after fixation at 3T (a & b) and 7T (c & d).

Unfortunately, due to the different stiffness between the fixed and unfixed kidneys, the same protocol did not deliver usable T_2^* maps as the unfixed kidney vibrated too much in the PBS. This problem could be reduced in future either by use of vibration insulation between the sample and scanner as per

6.4. Monitoring Changes in MR Parameters Post Fixation

Dawe *et al* [65] or by embedding the sample in agarose medium as per Kolk *et al* [66]. The largest changes in quantitative parameters occurred between twenty four hours and one week after fixation. After this the general trend is that the T_1 of the cortex and medulla converge and the T_2^* of the medulla remains relatively constant while the T_2^* of the cortex increases. There are hints that the T_2^* of the cortex is beginning to plateau by the end of the experiment. This indicates that, left for sufficiently long amounts of time, the tissue will reach a steady state, however in the first week, when the samples have a T_1 most similar to that of an unfixed kidney, the quantitative parameters measured will have a dependence on time and as such necessitates a standardisation in the protocol, specifically the time at which the samples are scanned.

It will be possible to scan most human samples within twenty four hours of fixation, as such it is desirable to ascertain how much T_1 , T_2^* and histology change over this period. Scanning was only performed at 3T as more frequent measurements were preferable to measurements at different field strengths. For this reason, the number of inversion and echo times used to generate the maps was reduced to five and six inversion/echo times respectively fit the protocol into one hour. The choice TI and TE was arrived at empirically by calculating maps with every combination of five/six previously acquired TI/TE and comparing the results to maps calculated using the full complement of time points. The reduced protocol consisted of acquisitions with TI of 400 ms, 500 ms, 750 ms, 900 ms, 1100 ms and 2600 ms and TE of 15 ms, 20 ms, 25 ms, 40 ms and 50 ms. The reduction in time points sampled resulted in a mean increase in T_1 of 21 ± 12 ms and T_2^* of 0.3 ± 1.2 ms compared to the fully sampled protocol.

Scanning sessions started at 1.5 hours, 2.5 hours, 4 hours, 5.5 hours, 19 hours and 22 hours after the sample was removed from the NBF. Due to the potential for relatively rapid changes in properties, especially T_1 , the order in which TI/TE were collected was randomised rather than ascending/descending order (however this order was kept consistent between scanning sessions). This means any changes in T_1/T_2^* over the 30/20 minute acquisition period

6.4. Monitoring Changes in MR Parameters Post Fixation

will manifest themselves and non-systematic noise and thus will simply increase the uncertainty in the fit rather than affecting the calculated value.

To investigate changes in histology over the same time period, the other kidney from the animal was biopsied at the start of each scanning session. Mason's trichrome and Haematoxylin and Eosin (H and E) staining was performed on these samples.

Variation in T_1 and T_2^* over the period being scanned is shown in Figure 6.26. No significant change in either T_1 and T_2^* was observed, the corresponding histology showed no change in the cortex however there was a noticeable inflammatory response in the medulla. This means that the ex-vivo protocol can be performed at any time in the first twenty four hours after fixation and as such makes future experimental logistics simpler.

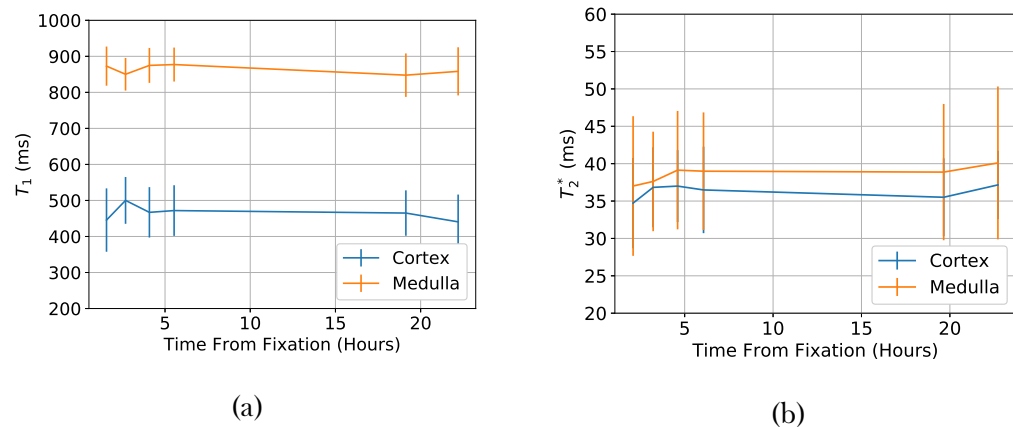


Figure 6.26: Changes in T_1 (a) and T_2^* (b) in the first twenty four hours a sample is stored in PBS after being fixed in NBF.

stagger
slightly
so
error
bars
are
vis-
ible

6.5 Correlating MRI Measures with Histology in Kidneys of Differing Ages

To verify correlation between MRI measurements and histology, kidneys were collected from a 0.5 year old and 2.5 year old pig. These different ages were expected to have differing levels of renal inflammation and fibrosis. T_1 and T_2^* maps were acquired from both samples and cortical biopsies were removed from the same animals for histological analysis.

Figure 6.27 shows example MRI data collected from these samples and Figure 6.28 shows the quantitative differences in T_1 and T_2 between the kidneys.

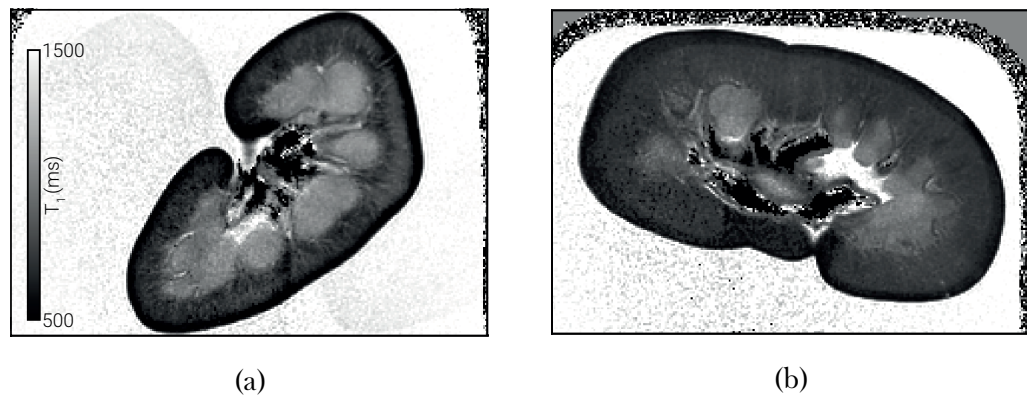


Figure 6.27: (a) T_1 map of a 0.5 year old pig kidney. (b) T_1 map of a 2.5 year old pig kidney.

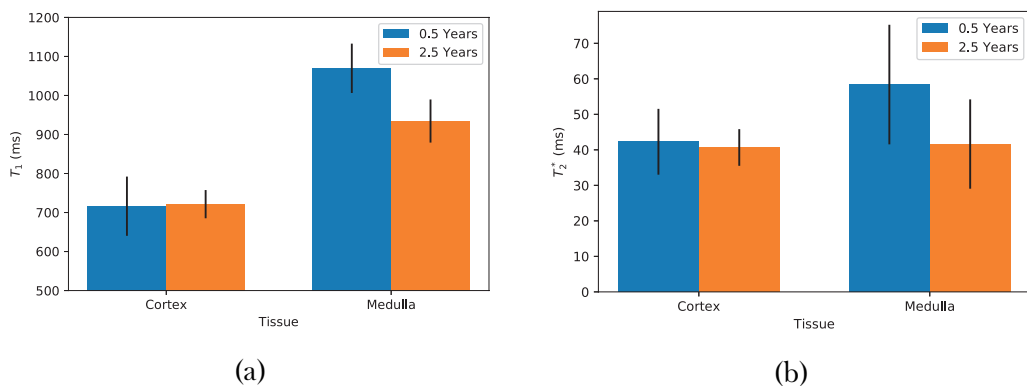


Figure 6.28: (a) The T_1 of the renal cortex and medulla of the two samples. (b) The T_2^* of the renal cortex and medulla of the two samples.

6.5. Correlating MRI Measures with Histology in Kidneys of Differing Ages

No significant change is observed in the T_1 or T_2^* of the cortex; the medulla of the older kidney does have a degreased T_1 . No significant differences were observed in the cortical biopsy samples. This shows agreement between the MRI and histology measurements as neither showed any change in the cortex.

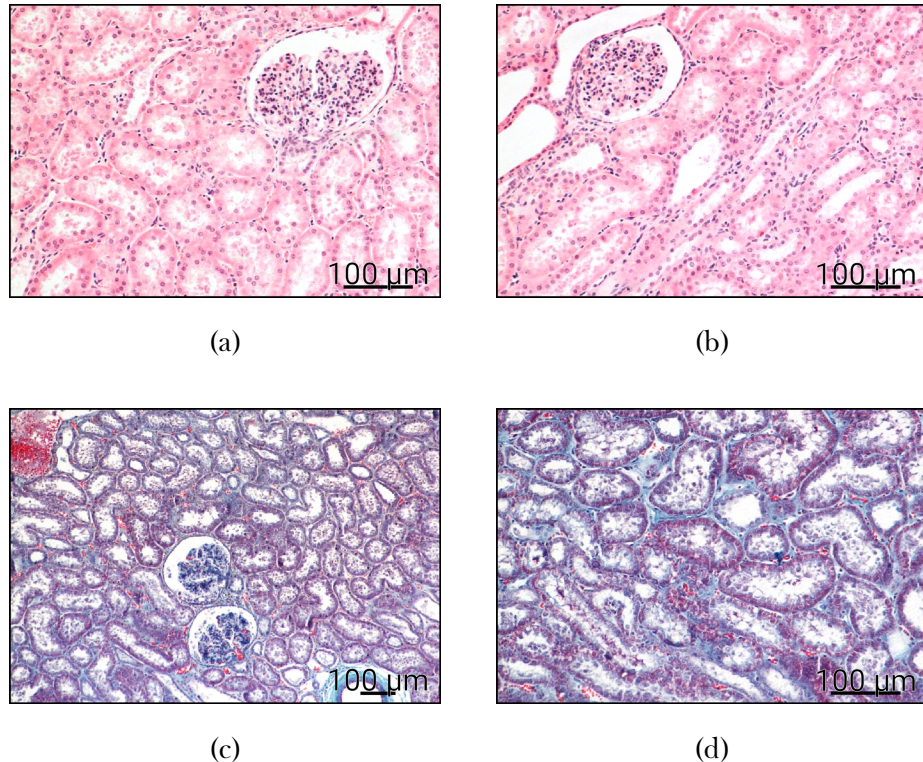


Figure 6.29: (a) A sample of renal cortex from a 0.5 year old pig stained with H and E. (b) A sample of renal cortex from a 2.5 year old pig stained with H and E. (c) A sample of renal cortex from a 0.5 year old pig stained with Masson's trichrome. (d) A sample of renal cortex from a 2.5 year old pig stained with Masson's trichrome.

To further investigate how T_1 changes with age, kidneys of 1 day old and 4 week old pigs were scanned and compared to histology. Due to their much smaller size, manually segmenting the cortex and medulla of these samples was not possible, as such the depth based analysis outlined in Section 6.3 was employed with a layer thickness of 0.5 mm.

Initially an assessment of consistency between kidneys of the same age was performed. T_1 maps were of three kidneys from two different animals

6.5. Correlating MRI Measures with Histology in Kidneys of Differing Ages

were generated i.e. both kidneys of one animal and the right kidney of another animal were scanned. In Figure 6.30 excellent agreement between all three kidneys can be seen, with an especially high correlation between kidneys from the same animal. This both gives confidence in the depth based analysis when applied to very small kidneys and indicates that there is a low degree of variance in kidneys of this age.

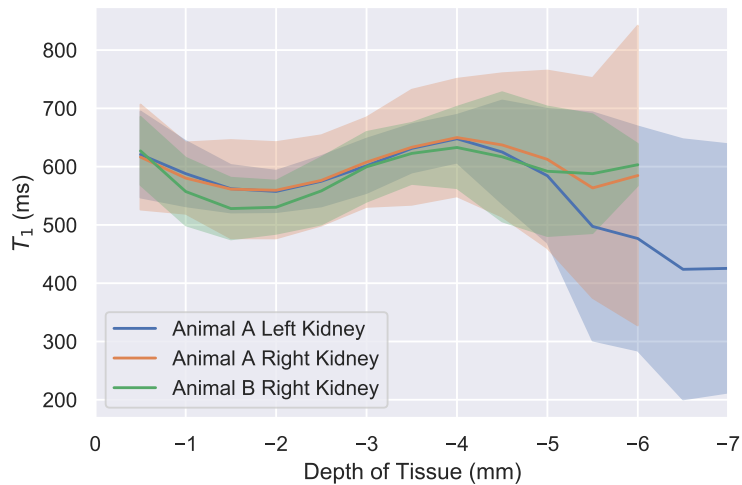


Figure 6.30: Changes in T_1 with renal tissue depth in kidneys of one day old pigs. The shaded area is the standard deviation within each 0.5 mm thick layer of tissue.

The same depth based analysis was applied to a 4 week old kidney and the 0.5 year and 2.5 year old kidneys analysed above. The changes in T_1 with depth are shown in Figure 6.31 both as absolute tissue depth in mm and relative tissue depth in percent, therefore normalising for kidney size. In this figure it can be observed that the T_1 of renal tissues differentiates with age. This is in part likely due to decreasing water content with age (~85% in neonatal kidneys, decreasing to ~65-70% by adulthood) and in part due to the lower glomerular density in younger kidneys.

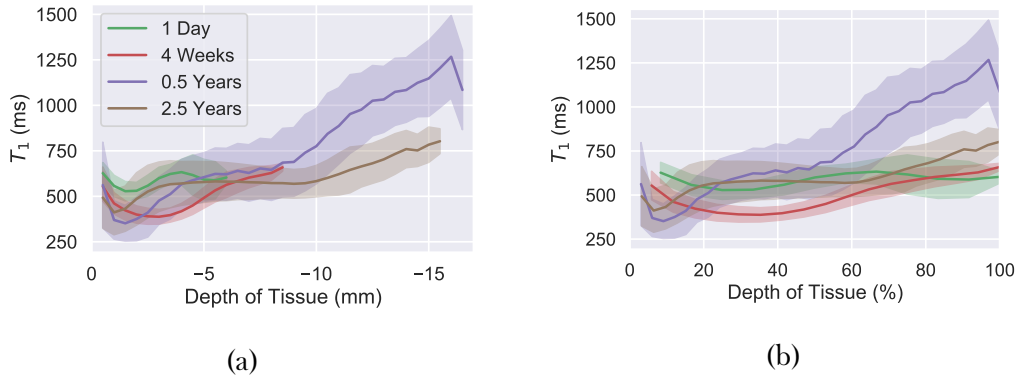


Figure 6.31: Changes in T_1 with renal depth of pig kidneys of multiple ages. The shaded area is the standard deviation within each 0.5 mm thick layer of tissue. (a) shows the absolute depth, (b) shows the relative depth with 0% being the surface of the kidney and 100% being the deepest tissue.

In future samples from older pigs should be scanned as these will have a greater degree of fibrosis. Procurement of these samples has proved more difficult as it is not common for pigs to be kept to older ages. Biopsy samples should also include medullary tissue for histological analysis as both Figure 6.25 and Figure 6.28 indicate that medullary tissue is relatively variable in quantitative MRI and as such, being able to correlate this with histology would be insightful.

6.6 Conclusion of Future Work

A paired ex-vivo and in-vivo quantitative renal MRI protocol has been developed to assess T_1 , T_2 , T_2^* , ADC and FA and tractography in the same organ both inside and outside the body. This protocol can be combined with histological analysis of the samples to link cutting edge MRI measures with existing standards for assessment of renal health. Understanding this link will enable MRI to augment the current practice of renal biopsies. The highly localised sampling of a biopsy followed by histology can be combined with MRIs whole organ coverage to give a better indication of the heterogeneity of

6.6. Conclusion of Future Work

renal health.

The ex-vivo part of the protocol could also be used in future to assist stratification of donated organs prior to transplant. Organ availability is the limiting factor in renal transplant rate, by increasing confidence in marginal quality organs the time a patient spends on the transplant waiting list could be reduced, reducing risks of complications for the patient due to extended time on dialysis and reduce cost to the health service. The in-vivo protocol could be used to proactively identify dysfunctional grafts and thus modify the course of treatment to extend the life of the transplant.

Further developments in this area will initially focus on validation of the ex-vivo protocol in a single kidney. By the nature of protocol development, not all aspects are developed at the same time. Unfortunately the Coronavirus pandemic of 2020 limited the availability of samples and access to scanners towards the end of protocol development. As such, the complete protocol has not been run on a single sample to collect and overlay all quantitative parameters. The correlation of histology and MRI data could also be improved. Currently, the histology and imaging data are not registered and as such voxel by voxel correlations with histology are not possible. Recently developed software packages focusing on the registration of histology and MRI data should assist with this aim [28].

Future developments will also explore the use of Arterial Spin Labelling (ASL) on perfused ex-vivo organs. Perfusion of kidneys while waiting for a recipient to be matched is an area of intense research [67–69]. ASL could be used to assess the success of these mechanical perfusion mechanisms and direct improvements in the procedure. Finally, an assessment of glomerular number and density via MRI would be an ideal comparison to certain histopathological metrics. While it is not possible to resolve individual glomeruli with the current protocol, other groups have recently had success applying deep learning and super resolution techniques to enable counting of the glomeruli in a sample at 3T.

6.7 Acknowledgements

We are grateful for access to the University of Nottingham's Augusta high performance computing service. We also thank Prof David Gardner of University of Nottingham Veterinary Science for his assistance with sample acquisition, histopathological processing of samples and general renal physiology expertise. Finally we wish to thank Kevin Aquino for his work developing 3D depth maps in the brain.

6.8 References

1. Daniel, A. J., Buchanan, C., Kazmi, I., Cox, E., Selby, N., Gardner, D. & Francis, S. *The Effects of Fixation and Age on Relaxometry Measurements of Ex-Vivo Kidneys* in *Proc. Intl. Soc. Mag. Reson. Med.* 27 International Society of Magnetic Resonance in Medicine Annual Meeting (Montreal, 13th May 2019).
2. Kazmi, I., Danial, A., Buchanan, C., Francis, S., Maarten W, T. & Nick, S. Determining Optimal Technique for Tissue Fixation for Ex-Vivo MRI Imaging of Porcine Kidneys. *Nephrology Dialysis Transplantation* **34**. doi:10.1093/ndt/gfz106.FP093 (gfz106.FP093 1st June 2019).
3. Nery, F., Daniel, A. J., Sousa, J. & Buchanan, C. *UKRIN Kidney Analysis Toolbox* version v0.1.0. UK Renal Imaging Network, Dec. 2020.
4. Daniel, A. J. et al. *UKRIN Kidney Analysis Toolbox (UKAT): A Framework for Harmonized Quantitative Renal MRI Analysis* in *Proc. Intl. Soc. Mag. Reson. Med.* 28 International Society of Magnetic Resonance in Medicine Annual Meeting. **29** (Online, May 2021), 2379.
5. Rathod, K. R., Popat, B. A., Pandey, A., Jamale, T. E., Hase, N. K. & Deshmukh, H. L. Safety and Effectiveness of Transjugular Renal Biopsy: A Single Center Study. *Indian Journal of Nephrology* **27**, 118–123 (2017).
6. Mal, F., Meyrier, A., Callard, P., Altman, J. J., Kleinknecht, D., Beaugrand, M. & Ferrier, J. P. Transjugular Renal Biopsy. *Lancet (London, England)* **335**, 1512–1513 (23rd June 1990).
7. Leung, G., Kirpalani, A., Szeto, S. G., Deeb, M., Foltz, W., Simmons, C. A. & Yuen, D. A. Could MRI Be Used To Image Kidney Fibrosis? A Review of Recent Advances and Remaining Barriers. *Clinical Journal of the American Society of Nephrology* **12**, 1019–1028 (7th June 2017).
8. Inoue, T. et al. Noninvasive Evaluation of Kidney Hypoxia and Fibrosis Using Magnetic Resonance Imaging. *Journal of the American Society of Nephrology: JASN* **22**, 1429–1434 (Aug. 2011).
9. Zhao, J., Wang, Z. J., Liu, M., Zhu, J., Zhang, X., Zhang, T., Li, S. & Li, Y. Assessment of Renal Fibrosis in Chronic Kidney Disease Us-

6.8. References

- ing Diffusion-Weighted MRI. *Clinical Radiology* **69**, 1117–1122 (Nov. 2014).
10. Feng, Q., Ma, Z., Wu, J. & Fang, W. DTI for the Assessment of Disease Stage in Patients with Glomerulonephritis - Correlation with Renal Histology. *European Radiology* **25**, 92–98 (1st Jan. 2015).
 11. Friedli, I. *et al.* New Magnetic Resonance Imaging Index for Renal Fibrosis Assessment: A Comparison between Diffusion-Weighted Imaging and T1 Mapping with Histological Validation. *Scientific Reports* **6**. doi:10.1038/srep30088. pmid: 27439482 (21st July 2016).
 12. Berchtold, L. *et al.* Validation of the Corticomedullary Difference in Magnetic Resonance Imaging-Derived Apparent Diffusion Coefficient for Kidney Fibrosis Detection: A Cross-Sectional Study. *Nephrology Dialysis Transplantation* **35**, 937–945 (1st June 2020).
 13. Jafari, R., Hectors, S. J., González, A. K. K. de, Spincemaille, P., Prince, M. R., Brittenham, G. M. & Wang, Y. Integrated Quantitative Susceptibility and R2* Mapping for Evaluation of Liver Fibrosis: An Ex Vivo Feasibility Study. *NMR in Biomedicine* **34**, e4412 (2021).
 14. Sabouri, S., Fazli, L., Chang, S. D., Savdie, R., Jones, E. C., Goldenberg, S. L., Black, P. C. & Kozlowski, P. MR Measurement of Luminal Water in Prostate Gland: Quantitative Correlation between MRI and Histology. *Journal of Magnetic Resonance Imaging* **46**, 861–869 (2017).
 15. Dhatt, R. *et al.* MRI of the Prostate With and Without Endorectal Coil at 3 T: Correlation With Whole-Mount Histopathologic Gleason Score. *American Journal of Roentgenology* **215**, 133–141 (11th Mar. 2020).
 16. Uribe, C. F., Jones, E. C., Chang, S. D., Goldenberg, S. L., Reinsberg, S. A. & Kozlowski, P. In Vivo 3 T and Ex Vivo 7 T Diffusion Tensor Imaging of Prostate Cancer: Correlation with Histology. *Magnetic Resonance Imaging* **33**, 577–583 (1st June 2015).
 17. Lazari, A. & Lipp, I. Can MRI Measure Myelin? Systematic Review, Qualitative Assessment, and Meta-Analysis of Studies Validating Microstructural Imaging with Myelin Histology. *NeuroImage* **230**, 117744 (15th Apr. 2021).

6.8. References

18. Peters, J. M. *et al.* White Matter Mean Diffusivity Correlates with Myelination in Tuberous Sclerosis Complex. *Annals of Clinical and Translational Neurology* **6**, 1178–1190 (2019).
19. Moll, N. M. *et al.* Multiple Sclerosis Normal-Appearing White Matter: Pathology–Imaging Correlations. *Annals of Neurology* **70**, 764–773 (2011).
20. Howard, A. F., Mollink, J., Kleinnijenhuis, M., Pallebage-Gamarallage, M., Bastiani, M., Cottaar, M., Miller, K. L. & Jbabdi, S. Joint Modelling of Diffusion MRI and Microscopy. *NeuroImage* **201**, 116014 (1st Nov. 2019).
21. Mollink, J. *et al.* White Matter Changes in the Perforant Path Area in Patients with Amyotrophic Lateral Sclerosis. *Neuropathology and Applied Neurobiology* **45**, 570–585 (2019).
22. Mottershead, J. P. *et al.* High Field MRI Correlates of Myelincontent and Axonal Density in Multiple Sclerosis. *Journal of Neurology* **250**, 1293–1301 (1st Nov. 2003).
23. Seewann, A. *et al.* Diffusely Abnormal White Matter in Chronic Multiple Sclerosis: Imaging and Histopathologic Analysis. *Archives of Neurology* **66**, 601–609 (1st May 2009).
24. Hametner, S. *et al.* The Influence of Brain Iron and Myelin on Magnetic Susceptibility and Effective Transverse Relaxation - A Biochemical and Histological Validation Study. *NeuroImage* **179**, 117–133 (1st Oct. 2018).
25. Stüber, C. *et al.* Myelin and Iron Concentration in the Human Brain: A Quantitative Study of MRI Contrast. *NeuroImage* **93**, 95–106 (1st June 2014).
26. Bagnato, F. *et al.* Untangling the R2* Contrast in Multiple Sclerosis: A Combined MRI-Histology Study at 7.0 Tesla. *PLOS ONE* **13**, e0193839 (21st Mar. 2018).
27. Reeves, C. *et al.* Combined Ex Vivo 9.4T MRI and Quantitative Histopathological Study in Normal and Pathological Neocortical Resections in Focal Epilepsy. *Brain Pathology* **26**, 319–333 (2016).

6.8. References

28. Huszar, I. N. *et al.* Tensor Image Registration Library: Automated Non-Linear Registration of Sparsely Sampled Histological Specimens to Post-Mortem MRI of the Whole Human Brain. *bioRxiv*, 849570 (26th Nov. 2019).
29. Huszar, I. N. *et al.* Automated Slice-to-Volume Registration between Histology and Whole-Brain Post-Mortem MRI in *Proc. Intl. Soc. Mag. Reson. Med.* 27 International Society of Magnetic Resonance in Medicine Annual Meeting (Montreal, 16th May 2019).
30. Watson, C. J. E., Johnson, R. J., Birch, R., Collett, D. & Bradley, J. A. A Simplified Donor Risk Index for Predicting Outcome After Deceased Donor Kidney Transplantation. *Transplantation* **93**, 314–318 (15th Feb. 2012).
31. Rao, P. S., Schaubel, D. E., Guidinger, M. K., Andreoni, K. A., Wolfe, R. A., Merion, R. M., Port, F. K. & Sung, R. S. A Comprehensive Risk Quantification Score for Deceased Donor Kidneys: The Kidney Donor Risk Index. *Transplantation* **88**, 231–236 (27th July 2009).
32. Burton, H., Iyamu Perisanidou, L., Steenkamp, R., Evans, R., Mumford, L., Evans, K. M., Caskey, F. J. & Hilton, R. Causes of Renal Allograft Failure in the UK: Trends in UK Renal Registry and National Health Service Blood and Transplant Data from 2000 to 2013. *Nephrology Dialysis Transplantation* **34**, 355–364 (1st Feb. 2019).
33. Szumowski, J., Durkan, M. G., Foss, E. W., Brown, D. S., Schwarz, E. & Crawford, D. C. Signal Polarity Restoration in a 3D Inversion Recovery Sequence Used with Delayed Gadolinium-Enhanced Magnetic Resonance Imaging of Cartilage (dGEMRIC). *Journal of Magnetic Resonance Imaging* **36**, 1248–1255 (1st Nov. 2012).
34. Branch, M., Coleman, T. & Li, Y. A Subspace, Interior, and Conjugate Gradient Method for Large-Scale Bound-Constrained Minimization Problems. *SIAM Journal on Scientific Computing* **21**, 1–23 (1st Jan. 1999).

6.8. References

35. Bjarnason, T. A. & Mitchell, J. R. AnalyzeNNLS: Magnetic Resonance Multiexponential Decay Image Analysis. *Journal of Magnetic Resonance* **206**, 200–204 (1st Oct. 2010).
36. Andersson, J. L. R., Skare, S. & Ashburner, J. How to Correct Susceptibility Distortions in Spin-Echo Echo-Planar Images: Application to Diffusion Tensor Imaging. *NeuroImage* **20**, 870–888 (1st Oct. 2003).
37. Le Bihan, D., Breton, E., Lallemand, D., Aubin, M. L., Vignaud, J. & Laval-Jeantet, M. Separation of Diffusion and Perfusion in Intravoxel Incoherent Motion MR Imaging. *Radiology* **168**, 497–505 (1st Aug. 1988).
38. Andersson, J. L. R. & Sotiroopoulos, S. N. An Integrated Approach to Correction for Off-Resonance Effects and Subject Movement in Diffusion MR Imaging. *NeuroImage* **125**, 1063–1078 (15th Jan. 2016).
39. Andersson, J. L. R. & Sotiroopoulos, S. N. Non-Parametric Representation and Prediction of Single- and Multi-Shell Diffusion-Weighted MRI Data Using Gaussian Processes. *NeuroImage* **122**, 166–176 (15th Nov. 2015).
40. Garyfallidis, E., Brett, M., Amirbekian, B., Rokem, A., Van Der Walt, S., Descoteaux, M. & Nimmo-Smith, I. Dipy, a Library for the Analysis of Diffusion MRI Data. *Frontiers in Neuroinformatics* **8**. doi:10 . 3389 / fninf . 2014 . 00008 (2014).
41. Wang, R., Benner, T., Sorensen, A. G. & Wedeen, V. J. *Diffusion Toolkit: A Software Package for Diffusion Imaging Data Processing and Tractography* in *Proc. Intl. Soc. Mag. Reson. Med.* 15 International Society of Magnetic Resonance in Medicine Annual Meeting (Aug. 2007), 8720.
42. Descoteaux, M., Angelino, E., Fitzgibbons, S. & Deriche, R. Regularized, Fast, and Robust Analytical Q-Ball Imaging. *Magnetic Resonance in Medicine* **58**, 497–510 (2007).
43. Hess, C. P., Mukherjee, P., Han, E. T., Xu, D. & Vigneron, D. B. Q-Ball Reconstruction of Multimodal Fiber Orientations Using the Spherical Harmonic Basis. *Magnetic Resonance in Medicine* **56**, 104–117 (2006).

6.8. References

44. Tournier, J. .-.D., Calamante, F., Gadian, D. G. & Connelly, A. Direct Estimation of the Fiber Orientation Density Function from Diffusion-Weighted MRI Data Using Spherical Deconvolution. *NeuroImage* **23**, 1176–1185 (1st Nov. 2004).
45. Tournier, J.-D., Calamante, F. & Connelly, A. Robust Determination of the Fibre Orientation Distribution in Diffusion MRI: Non-Negativity Constrained Super-Resolved Spherical Deconvolution. *NeuroImage* **35**, 1459–1472 (1st May 2007).
46. Tax, C. M. W., Jeurissen, B., Vos, S. B., Viergever, M. A. & Leemans, A. Recursive Calibration of the Fiber Response Function for Spherical Deconvolution of Diffusion MRI Data. *NeuroImage* **86**, 67–80 (1st Feb. 2014).
47. Garyfallidis, E. *Towards an Accurate Brain Tractography* Ph.D. (University of Cambridge, 2013).
48. Gürses, B., Kılıçkesmez, O., Taşdelen, N., Firat, Z. & Gürmen, N. Diffusion Tensor Imaging of the Kidney at 3 Tesla MRI: Normative Values and Repeatability of Measurements in Healthy Volunteers. *Diagnostic and Interventional Radiology (Ankara, Turkey)* **17**, 317–322 (Dec. 2011).
49. Jaimes, C., Darge, K., Khrichenko, D., Carson, R. H. & Berman, J. I. Diffusion Tensor Imaging and Tractography of the Kidney in Children: Feasibility and Preliminary Experience. *Pediatric Radiology* **44**, 30–41 (1st Jan. 2014).
50. Notohamiprodjo, M., Dietrich, O., Horger, W., Horng, A., Helck, A. D., Herrmann, K. A., Reiser, M. F. & Glaser, C. Diffusion Tensor Imaging (DTI) of the Kidney at 8 Tesla—Feasibility, Protocol Evaluation and Comparison to 1.5 Tesla. *Investigative Radiology* **45**, 245 (May 2010).
51. Thavarajah, R., Mudimbaimannar, V. K., Elizabeth, J., Rao, U. K. & Ranganathan, K. Chemical and Physical Basics of Routine Formaldehyde Fixation. *Journal of Oral and Maxillofacial Pathology : JOMFP* **16**, 400–405 (2012).
52. Self, M. W., van Kerkoerle, T., Goebel, R. & Roelfsema, P. R. Benchmarking Laminar fMRI: Neuronal Spiking and Synaptic Activity dur-

6.8. References

- ing Top-down and Bottom-up Processing in the Different Layers of Cortex. *NeuroImage* **197**, 806–817 (15th Aug. 2019).
53. Muckli, L., De Martino, F., Vizioli, L., Petro, L. S., Smith, F. W., Ugurbil, K., Goebel, R. & Yacoub, E. Contextual Feedback to Superficial Layers of V1. *Current Biology* **25**, 2690–2695 (19th Oct. 2015).
 54. Waehnert, M. D., Dinse, J., Weiss, M., Streicher, M. N., Waehnert, P., Geyer, S., Turner, R. & Bazin, P. .-L. Anatomically Motivated Modeling of Cortical Laminae. *NeuroImage. In-Vivo Brodmann Mapping of the Human Brain* **93**, 210–220 (1st June 2014).
 55. Taso, M., Munsch, F., Zhao, L. & Alsop, D. C. Regional and Depth-Dependence of Cortical Blood-Flow Assessed with High-Resolution Arterial Spin Labeling (ASL). *Journal of Cerebral Blood Flow & Metabolism*, 0271678X20982382 (14th Jan. 2021).
 56. Piskunowicz, M. *et al.* A New Technique with High Reproducibility to Estimate Renal Oxygenation Using BOLD-MRI in Chronic Kidney Disease. *Magnetic Resonance Imaging* **33**, 253–261 (1st Apr. 2015).
 57. Milani, B. *et al.* Reduction of Cortical Oxygenation in Chronic Kidney Disease: Evidence Obtained with a New Analysis Method of Blood Oxygenation Level-Dependent Magnetic Resonance Imaging. *Nephrology Dialysis Transplantation* **32**, 2097–2105 (1st Dec. 2017).
 58. Pruijm, M., Milani, B. & Burnier, M. Blood Oxygenation Level-Dependent MRI to Assess Renal Oxygenation in Renal Diseases: Progresses and Challenges. *Frontiers in Physiology* **7**. doi:10.3389/fphys.2016.00667. pmid: 28105019 (5th Jan. 2017).
 59. Li, L.-P., Milani, B., Pruijm, M., Kohn, O., Sprague, S., Hack, B. & Prasad, P. Renal BOLD MRI in Patients with Chronic Kidney Disease: Comparison of the Semi-Automated Twelve Layer Concentric Objects (TLCO) and Manual ROI Methods. *Magnetic Resonance Materials in Physics, Biology and Medicine*. doi:10.1007/s10334-019-00808-5 (10th Dec. 2019).

6.8. References

60. Bane, O. *et al.* Consensus-Based Technical Recommendations for Clinical Translation of Renal BOLD MRI. *Magnetic Resonance Materials in Physics, Biology and Medicine* **33**, 199–215 (1st Feb. 2020).
61. Dale, A. M., Fischl, B. & Sereno, M. I. Cortical Surface-Based Analysis: I. Segmentation and Surface Reconstruction. *NeuroImage* **9**, 179–194 (1st Feb. 1999).
62. Birkl, C., Langkammer, C., Golob-Schwarzl, N., Leoni, M., Haybaeck, J., Goessler, W., Fazekas, F. & Ropele, S. Effects of Formalin Fixation and Temperature on MR Relaxation Times in the Human Brain. *NMR in Biomedicine* **29**, 458–465 (1st Apr. 2016).
63. Schmierer, K. *et al.* Quantitative Magnetic Resonance of Postmortem Multiple Sclerosis Brain before and after Fixation. *Magnetic Resonance in Medicine* **59**, 268–277 (1st Feb. 2008).
64. Shatil, A. S., Uddin, M. N., Matsuda, K. M. & Figley, C. R. Quantitative Ex Vivo MRI Changes Due to Progressive Formalin Fixation in Whole Human Brain Specimens: Longitudinal Characterization of Diffusion, Relaxometry, and Myelin Water Fraction Measurements at 3T. *Frontiers in Medicine* **5**. doi:10.3389/fmed.2018.00031 (2018).
65. Dawe, R. J., Bennett, D. A., Schneider, J. A., Vasireddi, S. K. & Arfanakis, K. Postmortem MRI of Human Brain Hemispheres: T2 Relaxation Times during Formaldehyde Fixation. *Magnetic Resonance in Medicine* **61**, 810–818.
66. Kolk, A. G. van der *et al.* Imaging the Intracranial Atherosclerotic Vessel Wall Using 7T MRI: Initial Comparison with Histopathology. *American Journal of Neuroradiology*. doi:10.3174/ajnr.A4178. pmid: 25477359 (4th Dec. 2014).
67. Bellini, M. I., Charalampidis, S., Herbert, P. E., Bonatsos, V., Crane, J., Muthusamy, A., Dor, F. J. M. F. & Papalois, V. Cold Pulsatile Machine Perfusion versus Static Cold Storage in Kidney Transplantation: A Single Centre Experience. *BioMed Research International* **2019**, e7435248 (16th Jan. 2019).

6.8. References

68. Moers, C. *et al.* The Value of Machine Perfusion Perfusate Biomarkers for Predicting Kidney Transplant Outcome. *Transplantation* **90**, 966–973 (15th Nov. 2010).
69. Wight, J. P., Chilcott, J. B., Holmes, M. W. & Brewer, N. Pulsatile Machine Perfusion vs. Cold Storage of Kidneys for Transplantation: A Rapid and Systematic Review. *Clinical Transplantation* **17**, 293–307 (2003).

Appendix A

Tractography Pipeline

```
1 import numpy as np
2 import nibabel as nib
3 from dipy.tracking.eudx import EuDX
4 from dipy.tracking import utils
5 from dipy.tracking.streamline import Streamlines
6 from dipy.reconst import peaks
7 from dipy.reconst.csdeconv import \
8     ConstrainedSphericalDeconvModel, recursive_response
9 from dipy.core.gradients import gradient_table_from_bvals_bvecs
10 from dipy.io.streamline import save_trk
11
12 if __name__ == '__main__':
13     print('Ingesting Data')
14     img = nib.load('data.nii.gz')
15     mask = nib.load('mask.nii.gz')
16     bvals = np.loadtxt('bvals')
17     bvecs = np.loadtxt('bvecs')
18     data = img.get_fdata()
19
20     mask_data = mask.get_fdata()
21     mask_data = (mask_data>0)
22
23     gtab = gradient_table_from_bvals_bvecs(bvals.T, bvecs.T)
24
25     print('Estimating Fibre Response Function')
```

```
26     response = recursive_response(gtab, data,
27                                     mask=mask_data, sh_order=8,
28                                     peak_thr=0.01, init_fa=0.08,
29                                     init_trace=0.0021, iter=8,
30                                     convergence=0.001, parallel=False)
31
32     print('Generating CSD Model')
33     csd_model = ConstrainedSphericalDeconvModel(gtab, response,
34                                                   sh_order=6)
35
36     print('Getting Peaks From Model')
37     csd_peaks = peaks.peaks_from_model(model=csd_model,
38                                         data=data,
39                                         sphere=peaks.default_sphere,
40                                         relative_peak_threshold=.8,
41                                         min_separation_angle=45,
42                                         mask=mask_data)
43
44     print('Generating Seeds')
45     seeds = utils.seeds_from_mask(mask_data, density=1)
46
47     print('Propogating From Seeds')
48     streamline_gen = EuDX(csd_peaks.peak_values,
49                            csd_peaks.peak_indices,
50                            odf_vertices=peaks.default_sphere.vertices,
51                            a_low=.05, step_sz=.5, seeds=seeds)
52
53     print('Generating Streamlines')
54     streamlines = Streamlines(streamline_gen, buffer_size=512)
55
56     print('Saving Output For Your Perusal')
57     save_trk('tracts.trk', streamlines,
58              shape=mask.shape, vox_size=data.header.get_zooms(),
59              affine=data.affine)
```